Cell Reports
Physical Science

Article

An integrative approach to rational engineering of dengue virus-like particles

Graphical abstract

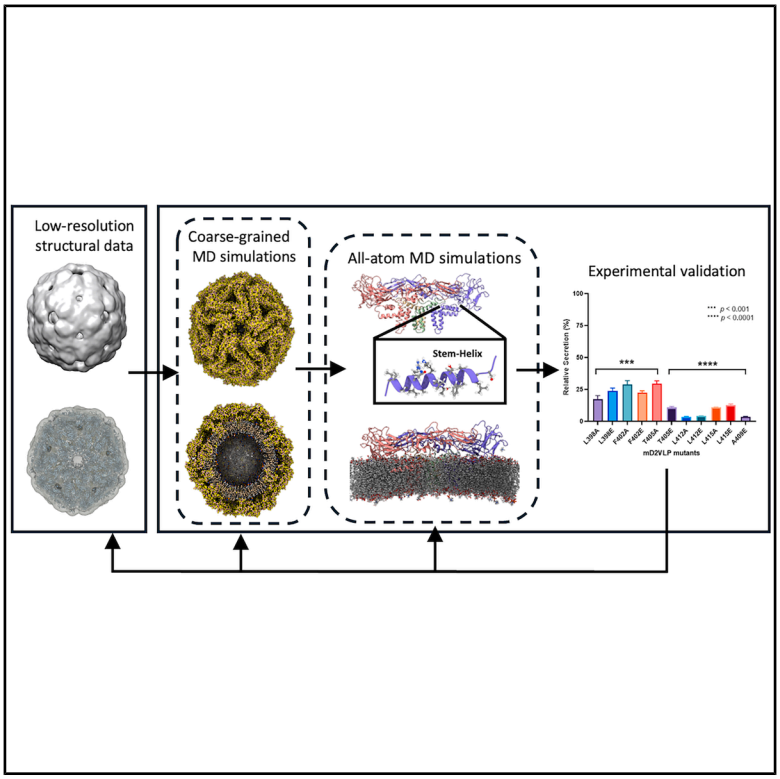

Authors

Venkata Raghuvamsi Palur, Fan-Chi Chen, Shang-Rung Wu, Guan-Wen Chen, Peter J. Bond, Day-Yu Chao, Jan K. Marzinek

Correspondence

dychao@dragon.nchu.edu.tw (D.-Y.C.), marzinekj@bii.a-star.edu.sg (J.K.M.)

In brief

Using multiscale simulations and experimental validation, this study uncovers how envelope protein-lipid interactions govern dengue virus-like particle (VLP) stability, secretion, and immunogenicity. The findings enable rational engineering of stable, homogeneous VLPs, advancing the development of next-generation dengue vaccines.

Highlights

- Multiscale modeling and lipidomics reveal factors shaping dengue VLP morphology
- E-protein stem helix-lipid interactions govern VLP stability, secretion, and immunogenicity
- Targeted mutations enhance dengue VLP yield, stability, and antibody recognition
- Integrative approach enables rational engineering of effective dengue VLP vaccines

Palur et al., 2025, Cell Reports Physical Science 6, 102814
September 17, 2025
https://doi.org/10.1016/j.xcrp.2025.102814

CellPress

Cell Reports
Physical Science

CellPress
OPEN ACCESS

Article

An integrative approach to rational engineering of dengue virus-like particles

Venkata Raghuvamsi Palur,[1,6] Fan-Chi Chen,[3,6] Shang-Rung Wu,[4] Guan-Wen Chen,[4] Peter J. Bond,[1,5] Day-Yu Chao,[2,3,*] and Jan K. Marzinek[1,7,*]

[1]Bioinformatics Institute (BII), Agency for Science, Technology and Research (A*STAR), 30 Biopolis Street, #07-01 Matrix, Singapore 138671, Republic of Singapore

[2]Graduate Institute of Microbiology and Public Health, College of Veterinary Medicine, National Chung Hsing University, Taichung City, Taiwan

[3]Microbial Genomics PhD Program, National Chung Hsing University and Academia Sinica, Taichung City, Taiwan

[4]School of Dentistry & Institute of Oral Medicine, College of Medicine, National Cheng Kung University, Tainan, Taiwan

[5]Department of Biological Sciences, National University of Singapore, Singapore, Singapore

[6]These authors contributed equally

[7]Lead contact

*Correspondence: dychao@dragon.nchu.edu.tw (D.-Y.C.), marzinekj@bii.a-star.edu.sg (J.K.M.)

https://doi.org/10.1016/j.xcrp.2025.102814

SUMMARY

Virus-like particles (VLPs) are promising vaccine candidates due to their noninfectious and highly immunogenic nature. Enveloped VLPs are unstable and heterogeneous in size because they lack a viral genomic core, yet they can induce a robust immune response. This motivates the characterization of their biophysical and structural properties to enable rational design of stable, highly immunogenic particles. We employed an integrative approach combining multiscale modeling, structural analyses, and *in vitro* experiments to gain molecular insights into the factors governing VLP stability, homogeneity, secretion, and antibody binding. We focused on dengue virus VLPs, which elicit neutralizing antibodies similar to infectious virions. Systematic introduction of mutations facing lipid tails in the stem helix of the chimeric E protein, guided by molecular simulations, allowed modulation of secretion efficiency and immunogenicity. Overall, this work highlights the role of envelope protein-lipid interactions in maintaining VLP stability and yield, guiding engineering of improved VLP-based vaccines.

INTRODUCTION

Dengue virus (DENV) is an enveloped virus that infects millions of people worldwide and significantly impacts human life and economies.[1,2] DENV belongs to the *Flaviviridae* family, a Flavivirus genus, which was recently renamed as *Orthoflavivirus*,[3] including several medically serious human pathogens, such as Zika virus (ZIKV), Japanese encephalitis virus (JEV), West Nile virus (WNV), and yellow fever virus (YFV). The outer layer of the ~50-nm-diameter virion is made of 180 copies of glycosylated envelope (E) and membrane (M) proteins embedded in the lipid bilayer, which encapsulate the ~10-kbp RNA genome in complex with the capsid protein. The ectodomain of the E protein contains three domains (DI, DII, and DIII), which lie flat on the viral membrane in the mature "smooth" virus (Figure 1). This sequence is followed by an α-helical stem region composed of three stem helices (SHs): E-helix 1 (E-H1) and E-H2 interacting with the lipid headgroups. Finally, a C-terminal transmembrane (TM) region containing two helices (TM1 and TM2) anchors the protein in the lipid bilayer. Immature DENV consists of 60 trimeric E and precursor M (prM) proteins, which form "spikes" emerging from the viral surface. In this state, each E-protein hydrophobic fusion peptide is capped with a precursor (pr) domain of prM protein, which prevents premature fusion of the virus. During the maturation process at low pH, accompanied by host furin protease-mediated prM cleavage, large-scale conformational changes in E proteins lead to a switch from noninfectious immature trimeric spikes to infectious mature dimers in smooth mature virions. Finally, mature DENV particles are secreted into the extracellular space.

There are four DENV serotypes (DENV-1 to -4) whose individual surface proteins and whole virus particle assemblies are nearly identical, and they share a sequence similarity of ~65%–70% at the entire genome level. During the viral life cycle, due to environmental factors such as pH, temperature, or the presence of divalent cations, the virus adopts numerous conformations with varying exposure of epitope sites.[4,5] Thereby, these complicate the efforts in dengue vaccine development to generate antibodies that neutralize all four serotypes. Meanwhile, the heterogeneity in viral morphologies[6] can also result in antibody-dependent enhancement (ADE), making it a challenge to develop highly potent and safe vaccines.[7–9] Unfortunately, current vaccines have not accounted for both challenges. For instance, Dengvaxia®, developed by Sanofi Pasteur, has low

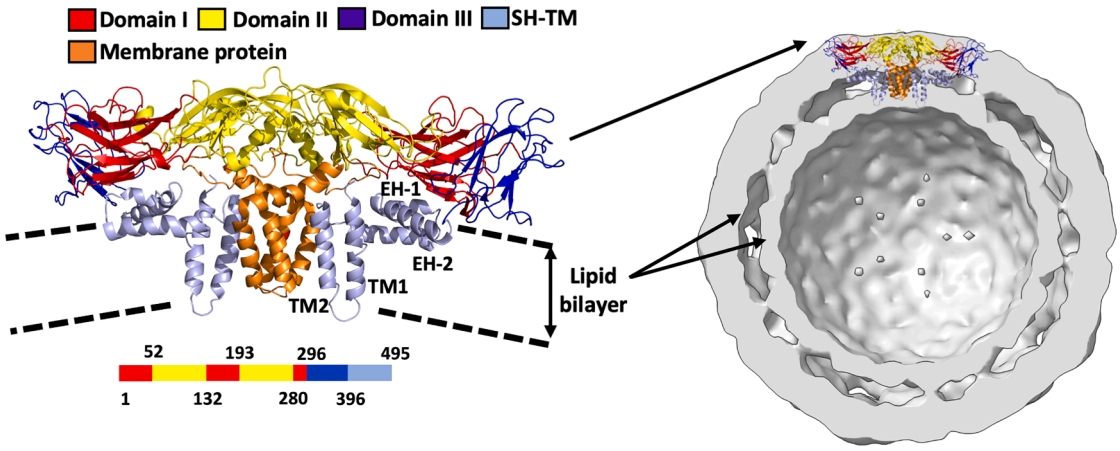

Figure 1. Dengue envelope and membrane protein dimer and its orientation within the VLP density map

A side view of the E/M protein dimer is shown in cartoon representation, with each E protein domain (DI, DII, and DIII) and the stem-helix-transmembrane (SH-TM) region highlighted in distinct colors (left). The dashed line indicates the approximate location of the lipid bilayer. The cross-section of the mature VLP density map (gray surface representation) with one dimer in the lipid bilayer is shown on the right. E, envelope; M, membrane.

efficacy and is associated with dangerous health outcomes among younger people or those without prior dengue infections after vaccination.[10,11] More recently, a tetravalent live attenuated vaccine developed by Takeda Pharmaceuticals Co., Ltd. (QDENGA®, TAK-003) was approved in Brazil for people regardless of prior dengue exposure.[12,13] Still, it was reported to show varying and waning efficacy among serotypes.[14] These factors make dengue vaccine development a major challenge from both an immunological and a structural point of view. Thus, there is an urgent need for novel and effective therapeutics.

Virus-like particles (VLPs) represent promising platforms for vaccine alternatives because they lack viral genomic material and hence are noninfectious, a key factor in vaccine safety.[15] VLPs are nanoparticles whose structures resemble those of viruses and can trigger significant immune responses, as shown by multiple US Food and Drug Administration (FDA)-approved vaccines and candidates in clinical trials.[16] Akin to viruses, VLPs can be classified as nonenveloped VLPs (neVLPs) or enveloped VLPs (eVLPs).[17] Unlike eVLPs, engineering neVLPs has achieved considerable success by manipulating the selectivity of cargo, stability, and homogeneity in particle assemblies.[18–20] The mature DENV-2 VLP was previously reported to induce broad neutralizing antibodies against all four DENV serotypes.[21] A more recent study of a tetravalent dengue VLP-based vaccine revealed that the vaccine generates neutralizing antibodies against all serotypes in nonhuman primates.[22] In contrast to dengue virions, mature dengue VLPs are only ~26–36 nm in diameter and are composed of 30 E and M protein dimers embedded within lipid vesicles. Previously, the cryoelectron microscopy (cryo-EM) density map of mature dengue serotype 2 VLP was solved at ~13-Å resolution (Figure 1).[21] To improve VLPs' secretion, the last 20% of the sequence (SH-TM region: residues 395–495) was replaced with that from JEV.[23] The VLP particle was shown to be a T = 1 icosahedral symmetry with a smooth surface. However, due to the absence of RNA and capsid proteins, the current cryo-EM mD2VLP data has low resolution because of the high heterogeneity of VLPs morphology with missing structural details such as secondary structure of the SH-TM region at the protein-lipid envelope interface. These complicate the engineering of DENV VLPs with desirable physicochemical properties and optimal protein-lipid interactions.

Extensive efforts have been directed toward engineering VLPs with desirable biophysical and immunological properties. As mentioned earlier, chimeric VLPs were previously generated with sequences corresponding to the ectodomain of DENV-2 and stem-TM regions of either JEV or vesicular stomatitis virus to increase the secretion and production of VLPs.[23,24] Higher secretion of DENV-2 and ZIKV VLPs in mammalian cells was previously shown via introducing F108A mutation at the fusion loop.[25] Nonetheless, to date, no study has investigated VLPs formation and stability in the context of interaction with the lipid bilayer.

In this work, we integrate experimental and computational techniques to identify critical protein-lipid interactions to engineer stable and homogeneous VLPs with improved secretion and retained immunogenic properties. We focused on chimeric mature dengue serotype 2 VLP (DENV-2 ectodomain residues 1–394, JEV stem-TM residues 395–495, hereafter referred to as mD2VLP), which has been shown to lead to highly immunogenic responses in mice.[21] First, we performed mass spectrometry (MS)-based lipidome profiling to determine the lipid composition of VLPs from different cell lines. Guided by the cryo-EM density map of mD2VLP, we constructed all-atom (AA) models and performed extensive molecular dynamics (MD) simulations to probe the protein-lipid and protein-protein interactions between E and M dimers governing particle stability. We specifically focused on mutations in the helical region E-H1, which is located near the lipid headgroups of the outer leaflet of the bilayer. We chose residues on the helix that point toward the lipid tails to strengthen protein-lipid interactions. These residues are located beneath the E-protein ectodomain, ensuring that the mutations do not affect epitope exposure (Figure 1). *In silico* mutations, through a set of AA MD simualtions, showed stronger protein-lipid interactions. These results were validated

by site-directed mutagenesis experiments in which substantial increases in VLP secretion were observed. The best-secreting double mutant provided with stable and homogenous particles, as revealed by cryo-EM, and remained equally immunogenic *in vitro* as reflected by monoclonal antibody (mAb) and polyclonal antibody (pAb) binding. Finally, coarse-grained (CG) simulations of the dengue VLPs reproduced particle morphologies that closely resembled cryo-EM micrographs, while the observed dynamics revealed the basis for VLP heterogeneity in solution. Overall, this work lays a general foundation for the rational development of highly secreting and effective VLPs for the use in next-generation vaccines.

RESULTS

The lipid composition of VLPs is conserved across orthoflaviviruses and cell lines

We first sought to characterize the lipid content of VLPs derived from several orthoflaviviruses under different conditions. We produced VLPs from different cell lines, and the lipidomic profiles of VLPs from each cell line were identified. Three different purified VLPs were used: (1) dengue mD2VLP prepared from both HEK293T and COS-1 cells, (2) JEV VLP (JEVLP) prepared from COS-1 cells, and (3) ZIKV-VLP (ZIKAVLP) prepared from COS-1 cells. The VLPs were purified and the particle formation confirmed by electron microscopy (EM) analysis (Figures 2A–2D). Also, the purified VLPs were subjected to lipid extraction followed by liquid chromatography-tandem MS (LC−MS/MS) to obtain lipidomic data. Detailed descriptions of VLP production, purification, lipid extraction, and LC-MS/MS can be found in the methods section (Figure S1). The results of LC-MS/MS analysis revealed similar lipid compositions across different orthoflavivirus VLPs from the same cell lines or the same VLPs from various cell lines. The two types of lipids extracted in the highest quantity from purified VLPs were diacylglycerols (DGs) in the glycerolipid category and fatty acids (FAs) in the fatty acyls category; these are mainly unsaturated FA chains with DG oxidized on carbon number 34 and FAs oxidized on carbon number 18. Phosphatidylcholine (PC), a glycerophospholipid; oxidized FAs (OxFAs), a fatty acyl; and other lipids, such as ceramide alpha-hydroxy FA-phytosphingosine (cerAP), in the sphingolipid category, had relatively low abundances (Figure 2E). By summing all the *m/z* spectra of the positive or negative lipids, no differences in the total amount of lipids were observed among the different types of VLPs (Figures 2F and 2G), indicating the amounts of purified VLP injected for LC-MS/MS analysis and the lipid compositions of different purified VLP were consistent.

Specific E-protein−lipid interactions govern VLP secretion efficiency

Previous studies have shown that the secretion of mD2VLPs following the transfection of prM/E plasmids into mammalian cells can be achieved only with an E-protein chimera (Echi), in which residues 395–495 of DENV-2, representing the SH-TM region, are replaced with that from JEV[23] (Figure 3A). We hypothesized that E-H1 may play a crucial role in VLP stability and secretion via interactions with the lipid envelope. Through helical wheel analysis of E-H1, we identified several amino acids, in particular, residues L398, F402, T405, A409, L412, and L415 that are facing the lipid bilayer (Figures 3B and 3C). To assess the contribution of these residues to VLP secretion, we performed site-directed mutagenesis at each site to alanine (A) or glutamate (E) to interrupt the interaction with the lipid bilayer (E-H1 mutants). The rationale of choosing A or E was to probe the effect of side-chain removal or introducing a negative charge at the negatively charged lipid-head-group region, both of which can potentially lower VLP secretion. The mutant plasmids were transfected into HEK293T cells to investigate changes in the relative VLP secretion efficiency with respect to that of the wild-type plasmid through antigen-capture enzyme-linked immunosorbent assay (ELISA). The results revealed that all the mutations had negative effects on VLP secretions. Among them, mutations at A409E and L412A/E had the greatest impact, with a P/N ratio close to 1 indicating no secretion (Figures 3D and 3E). An immunofluorescence assay (IFA) confirmed that E proteins accumulated within the cytoplasm of the cells (Figure S2). This shows the importance of the E-H1 helix in VLP assembly and highlights the critical sites that possibly modulate VLP secretion through the interaction of E-H1 residues facing the lipid bilayer.

To gain mechanistic insights into the effects of the mutations on VLP secretion, we performed a series of 500-ns-long all-atom MD (AA-MD) simulations of the dimeric DENV Echi protein of mD2VLP, embedded in biologically relevant lipid membrane models as well as E-H1 mutants. All the systems were embedded in two different membranes (Figures 4A and 4B), namely (1) a phospholipid-dominant (PL) lipid membrane (POPC:POPE:POPS) (POPC:phosphatidylcholine (16:0/18:1), POPE:phosphatidylethanolamine (16:0/18:1), and POPS:phosphatidylserine (16:0/18:1)) at a 6:3:1 ratio derived from an insect cell line from the work of Zhang et al.[26]; and (2) a diacylglycerol-dominant (DG) lipid membrane consisting of DG:SAPC:FA (DG: diacylglycerol (18:0/20:4), SAPC:phosphatidylcholine (18:0/20:4), and FA:FA (18:1)) at a 56:28:6 ratio (Figures 4A and 4B) derived from the lipidomics in this study. We first calculated the root-mean-square deviation (RMSD) and root-mean-square fluctuation (RMSF) of each E-M complex for Echi and each E-H1 helix mutant to establish the varying effects of point mutations on the overall dynamics (Figure S3). The RMSD values averaged over the last 100 ns of the simulations showed that the mutations did not have a significant effect on the overall protein complex structure compared to that of the Echi system (Figures 4C and 4D; Video S1). However, at the local level, analysis of the per-residue secondary structure and RMSF of the E-H1 helix during the simulation revealed that the F402E and A409E mutants and, to a lesser extent, L412E exhibited partial unfolding around residues 397–413 (Figures S4 and S5; Video S2). The unfolding usually applied to one of two E-H1 monomers only while many of them were short-lived. To assess the convergence of these changes we performed block analysis of E-H1 hydrogen-bond lifetimes as well as percentage change in the number of hydrogens bonds of helical backbone with respect to the experimental coordinates at 100-ns intervals (Figures S9A and S9B). We focused on experimentally derived DG-dominant lipid bilayer, and we observed that simulations converged in the last 200–300 ns in all cases except L412E. To improve the

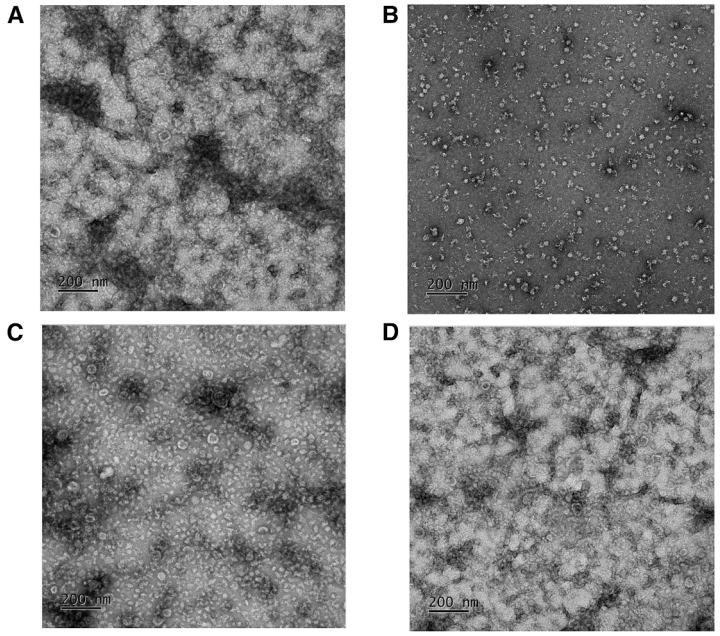

E

VLP	Cell type	Major lipid types	Number of carbons	Lipid ratio	% saturated
mD2VLP	COS-1	DG	34	19	28
		FA	18	9	0
		PC	30	3	52
		oXFA	18	1	16
mD2VLP	HEK293T	DG	34	19	24
		FA	18	9	0
		PC	34	3	0
		oXFA	18	1	15
ZIKAVLP	COS-1	DG	34	31	25
		FA	18	15	0
		PC	18	2	15
		oXFA	34	1	0
JEV-VLP	COS-1	DG	34	64	26
		FA	18	27	0
		PC	18	4	16
		oXFA	34	1	2

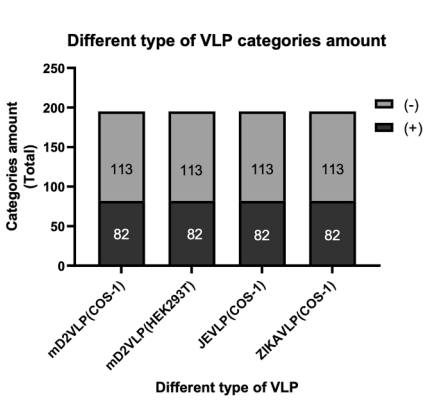

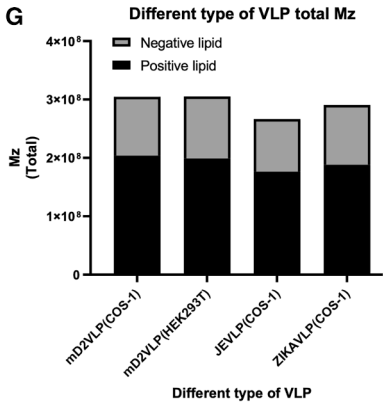

Figure 2. Particle formation and lipidomic analysis of four different orthoflavivirus VLPs via cryo-EM and LC-MS/MS analysis

(A–D) Representative EM images examined after different orthoflavivirus VLP purification from (A) mature DENV-2 VLPs (mD2VLPs) secreted from stable HEK293T cells and (B) Japanese encephalitis virus VLPs (JEVLP), (C) mD2VLPs, and (D) Zika virus VLPs (ZIKA-VLPs) generated from transiently transfected COS-1 cells.

(E) Lipid composition extracted from different VLPs. The total sum of the *m/z* spectra of all lipid categories detected from purified mD2VLPs was calculated from both the positive and negative ion scanning modes. To avoid the contamination of the lipid from HEK293T or COS-1 cells, the culture supernatants of the non-transfected cells were used as the control for the lipid extraction. Peaks were compared between VLP samples and controls, and only those with intensities at least 3-fold higher in VLPs were selected for lipidomic analysis using the LIPID MAPS database. Note that not all the *m/z* peaks can be mapped to the lipid categories after searching the lipid database. For lipid ratio calculations, only the four most abundant lipid types were considered, and values were normalized using the lipid type with the lowest *m/z* ratio as a reference (set to 1). DG, diacylglycerols; FA, fatty acid; PC, phosphatidylcholine; OxFA, oxidized fatty acid.

(F) The total amount of all mapped lipid categories detected from different purified VLPs based on positive (+) and negative (−) ion modes.

(G) The total *m/z* ratio of positive or negative lipids of all lipid categories detected from different purified VLPs. No differences in total amount or *m/z* were found among the different VLPs. The equivalent sums of either *m/z* spectra or lipid categories across different purified VLP indicated that the amounts of purified VLP injected for LC-MS/MS analysis or the lipid compositions of different purified VLP were consistent.

CellPress
OPEN ACCESS

A

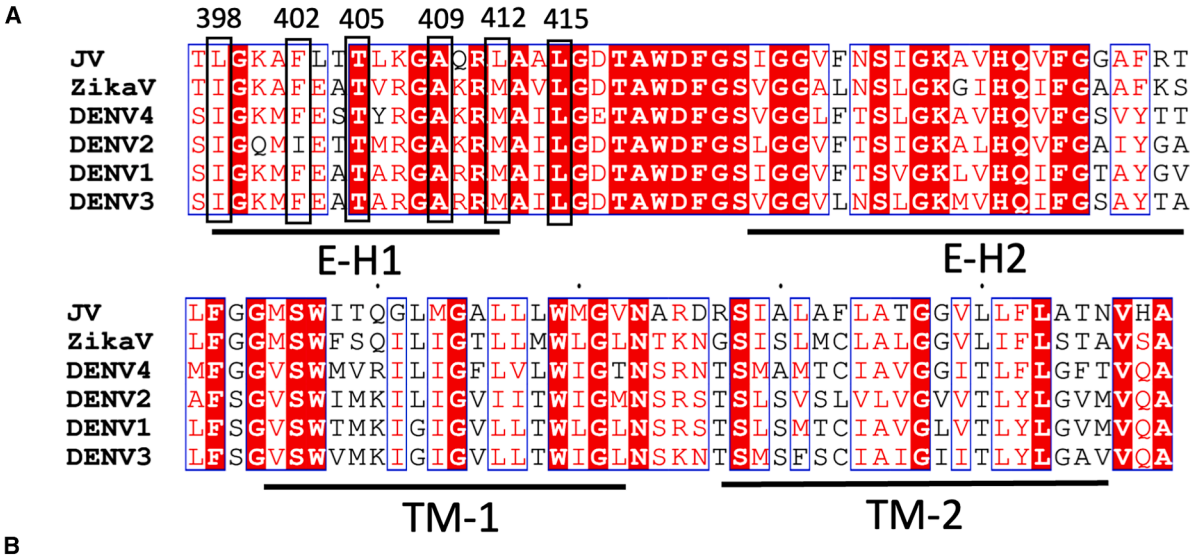

B

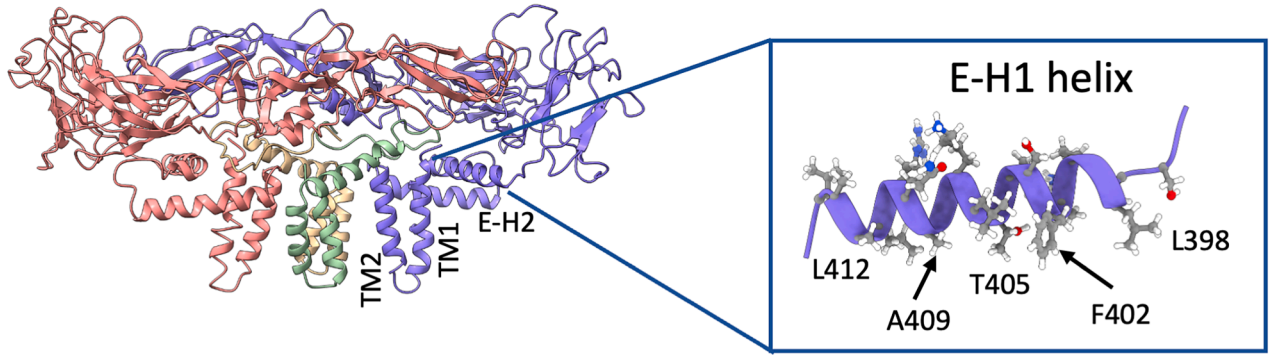

C

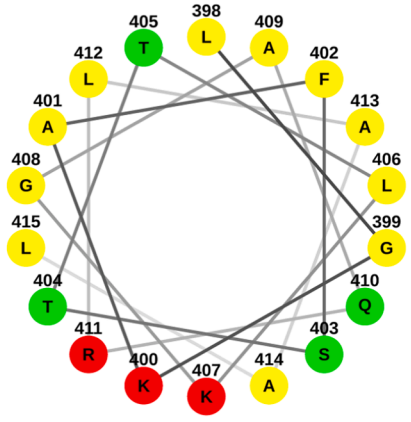

D

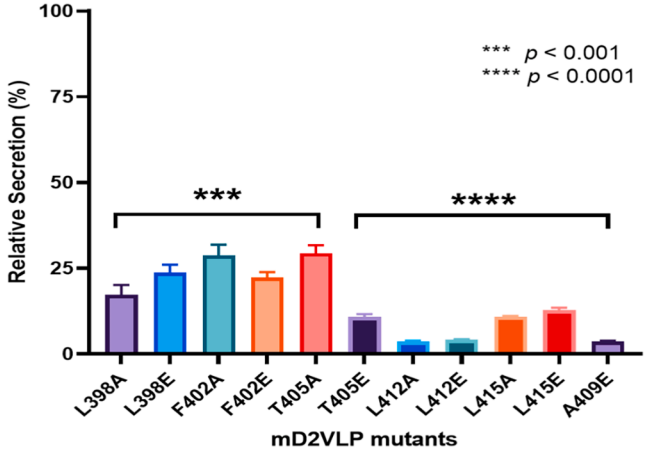

E

Group	L398A	L398E	F402A	F402E	T405A	T405E	L412A	L412E	L415A	L415E	A409E	mD2VLP
OD	0.28	0.39	0.47	0.37	0.48	0.18	0.06	0.07	0.18	0.21	0.06	1.64
P/N	5.48	7.48	9.10	7.06	9.30	3.41	1.15	1.33	3.45	4.04	1.15	31.66

(legend on next page)

sampling of this system, we have extended the simulation to 1,000 ns, which allowed for these values to converge (Figure S9C). Nevertheless, the percentage change in helical structure of E-H1 over the simulation time for all systems did not significantly differ from the unmutated Echi.

We next analyzed the interactions of the E-H1 helices with lipids, which showed that Echi exhibited a greater number of lipid contacts than did any of the A or E mutants (Figures S6A, S6B, and S7). This was the case for both the PL- and DG-dominant lipid membrane systems. Subsequent calculation of the per-residue membrane insertion depth with respect to the lipid head groups revealed that the E-H1 helices of Echi were buried more deeply into the bilayer than any of the other mutants (Figures S6C and S8) for both lipid compositions. Overall, this comparative analysis of Echi and E-H1 mutants provides the rationale of the reduction in secretion efficiency of VLPs observed in *in vitro* experiments, which arises from local loss of E-H1 helix-lipid interactions and, in selected cases, insignificant E-H1 unfolding.

E-H1 helix engineering to enhance VLP secretion

In an attempt to increase VLP secretion efficiency, we next aimed to identify mutations in the E-H1 helix that may enhance lipid envelope interactions without drastically perturbing the E-protein. We focused on mutations at critical sites along the E-H1 helix, which were observed to influence VLP secretion (Figure 4). In parallel, we used the Rosetta Membrane Proteins (RosettaMP) module[27] to calculate the difference in free energy between Echi and single mutants. An E-H1 mutational scan was performed at each site of interest, i.e., residues 402, 405, and 409 (sites 398 and 412 are hydrophobic residues), with all amino acids excluding proline across each site (Figures 5A and 5B). The mutation to leucine had the most favorable (negative) change in $\Delta\Delta G$, indicating that this mutation may result in a stabilizing effect (Figure 5B). To validate this result, we performed VLP secretion assays with single leucine (F402L, T405L, and A409L), double-leucine (F402L/T405L, T405L/A409L, and F402L/A409L), and triple-leucine (F402L/T405L/A409L) mutations on in the E-H1 of mD2VLP. Strikingly, both double- and triple-leucine mutant mD2VLPs produced ~2-fold greater secretion in comparison to mD2VLP (Figure 5C). Interestingly, despite favorable $\Delta\Delta G$ predictions by RosettaMP, single mutations showed negligible effect on VLP secretion *in vitro* (Figure 5C), highlighting the complexity of the secretion process and indicating that hybrid-empirical $\Delta\Delta G$ prediction alone cannot fully explain VLP secretion. Consistent with these findings, 500-ns AA-MD simulations of the double- or triple-leucine mutants of the Echi protein dimer of mD2VLP in a DG-dominant lipid bilayer revealed a stable and folded E-H1 helix with increased E-H1 lipid interactions and deeper helix insertions into the lipid bilayer (Figure S10 and Video S3).

To further validate the results of enhanced secretion of engineered VLPs, we picked the double (F402L/A409L and T405L/A409L) and triple mutants (F402L/T405L/A409L) to investigate the secretion kinetics on a daily basis. The results showed that all three mutant VLPs had significantly higher antigen expression levels starting from day 5 compared to the mD2VLP. Among them, the F402L/A409L mutant exhibited the highest secretion level, with a marked increase observed starting from day 5 (Figure 5D). Additionally, while antigen levels in the mD2VLP group began to decline noticeably on days 6 and 7, the mutant VLPs maintained robust antigen levels in the culture supernatant, suggesting that these mutations might contribute to improve both secretion and stability (Figure 5D). These findings support that the critical interactions between the E-H1 helix and the lipid envelope govern the secretion efficiency of DENV VLPs and that this effect may be rationally improved via targeted point mutations.

E-H1-helix mutations enhance the homogeneity of VLPs morphology

Further, to assess the effect of secretion-enhancing mutations on the overall structure of VLPs, we performed cryo-EM on mD2VLP as well as the highest secreting F402L/A409L double mutant. The purified VLP samples were prepared as described in the methods section and our previous work.[21,28] We observed significant differences in overall size distribution and morphology between the two VLP samples (Figure 6). Firstly, when looking at cryo-EM micrographs, the double mutant shows a higher proportion of spherical particles compared to mD2VLP (Figures 6A and 6D). We compared particle size distribution (Figures 6B–6E) and 2D-class averages (Figures 6C and 6F) of double-mutant and mD2VLP VLP micrographs. In the case of the double mutant, a single dominant particle size (30–32 nm) based on 2D-class average consisting of ~46% of total particles count was observed (Figure 6F). In contrast, the major dominant particle size of mD2VLP, also 30–32 nm, only consisted of ~33% (Figure 6C). This indicates that secretion-enhancing mutations contribute to producing homogenous particles as a result of enhanced envelope protein-lipid interactions. To further confirm the morphology homogeneity attained in double-mutant VLPs, the purity of mD2VLP and double-mutant mD2VLP was characterized by running SDS-PAGE. The results showed that the E protein was detected at approximately 50 kDa, as estimated

Figure 3. E-H1 mutations influence the VLP secretion *in vitro*

(A) Amino acid alignment of the transmembrane domain of four serotypes of dengue virus (DENV1–4), Japanese encephalitis virus (JEV), and Zika virus (ZIKV).
(B) A cartoon representation of the side view of the E-M protein dimer. The inset shows the magnified E-H1 helix and the amino acid side chains facing the membrane (liquorice representation).
(C) Helical wheel analysis of the transmembrane domain of E-H1 from the JEV E protein.
(D) The mD2VLP and site-specific mutated DNA plasmids were transfected into HEK293T cells by PEI. The respective VLP secretion was determined from the culture supernatant 5 days post transfection by antigen-capture ELISA. The relative secretion level of the respective mutant VLP was calculated as the percentage in comparison with the mD2VLP. Data are presented as the mean ± standard deviation (SD) of three independent experiments. Statistical analysis was performed using GraphPad Prism, with one-way ANOVA revealing a highly significant difference among the mutant VLPs.
(E) Summary table of the optical density (OD) and positive-to-negative OD (P/N) ratios for the different mutant VLPs. Notably, certain mutants demonstrated markedly decreased secretion levels with P/N ratio close to 1, compared to others, underscoring the functional impact of these mutations.

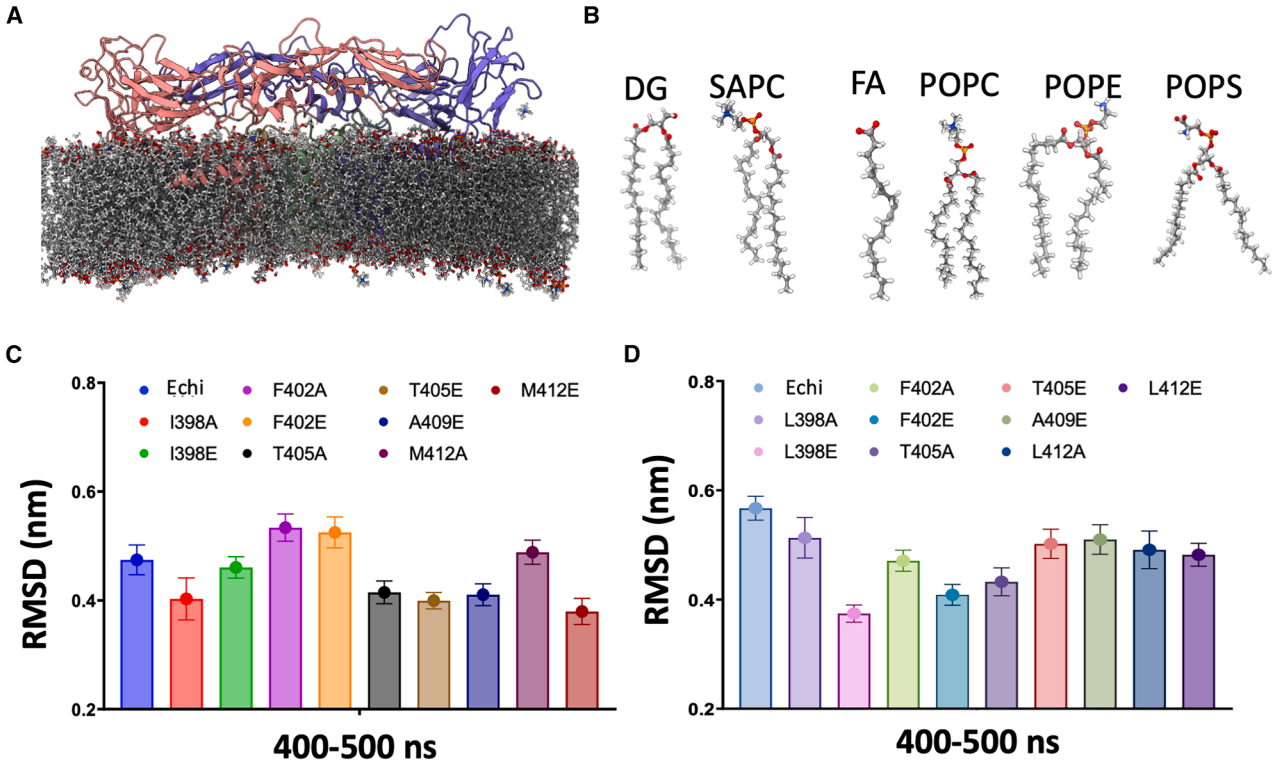

Figure 4. The effect of mutations on the E-H1 helix was assessed using AA-MD simulations of chimeric E-M protein dimers embedded in two different lipid bilayer compositions

(A) AA model of the E-M protein dimer embedded in the lipid membrane. The dominant lipid molecules found in the viral lipid envelope are shown in the liquorice representation.

(B–D) (B) The mean protein backbone RMSD over the final 100 ns of 500-ns-long simulation trajectories is shown for Echi and E-H1 helix mutants embedded in (C) PL-dominant (POPC:POPE:POPS) and (D) DG-dominant (DG:SAPC:FA) lipid membranes. Error bars represent standard deviations calculated over the last 100 ns of the simulation.

by ImageJ with different concentrations of bovine serum albumin (BSA) as reference (Figure S11). The comparable purity of the E-protein ratio of 1:1 confirms that the differences in VLP morphology is not due to the different amount of E protein assembled. In summary, the mD2VLP sample displayed significant size and shape variability among the particles, consistent with observations reported by Shen et al.[21] In contrast, the double-mutant sample exhibits a single size peak, indicating more uniform particles with clear symmetry, suggesting tightly packed proteins on the particle surface.

Further, we compared the epitope accessibility between mD2VLP and F402L/A409L double mutant to evaluate if the mutations on E-H1 affect the structural integrity and immunogenicity. We first normalized the amount of mD2VLP and double mutant to be equal based on the equivalent P/N ratio of the binding ELISA using DENV-2 pAb derived from mouse hyperimmune ascitic fluid (D2-MHIAF) as described in our previous study.[21] Subsequently, a panel of well-characterized murine mAbs, recognizing different domains of E protein, was used to map the epitopes expressed on mD2VLP and double mutant.[21] Notably, in the group treated with domain-specific mAbs, the mutant antigens were recognized more prominently than the mD2VLPs (Figure 6G; Table S3). This suggested that introduced mutations did not impair epitope exposure and may have improved antibody accessibility by enhancing homogeneity as shown in Figures 6D–6F and conformational stability. Next, we incubated both mD2VLP and double-mutant (F402L/A409L) VLPs at a wide range of temperatures (i.e., 37°C, 28°C, 4°C, −20°C, and −80°C) followed by antigen-capture ELISA using D2-MHIAF pAb for detection. Consistently among all the temperature conditions tested, the representative double mutant showed a higher stability to be captured on the ELISA plate, compared to mD2VLP, which degraded significantly, particularly at 37°C (Figure 6H). This shows the stabilizing effect of mutations that enhance E-protein-lipid interactions in overall particle stability. These results further support the potential advantages of the mutant in antigen presentation and immune recognition.

CG modeling of mature VLPs

Previous studies have shown that antibodies can target epitope sites on the E-protein monomer or dimer or across more complex quaternary sites on the orthoflavivirus particle surface.[8] Epitope exposure is a crucial variable among vaccine candidates that governs the magnitude of the host immune response.[21] Therefore, we constructed a fully assembled model of the mature VLP to gain insight into epitope exposure in the context

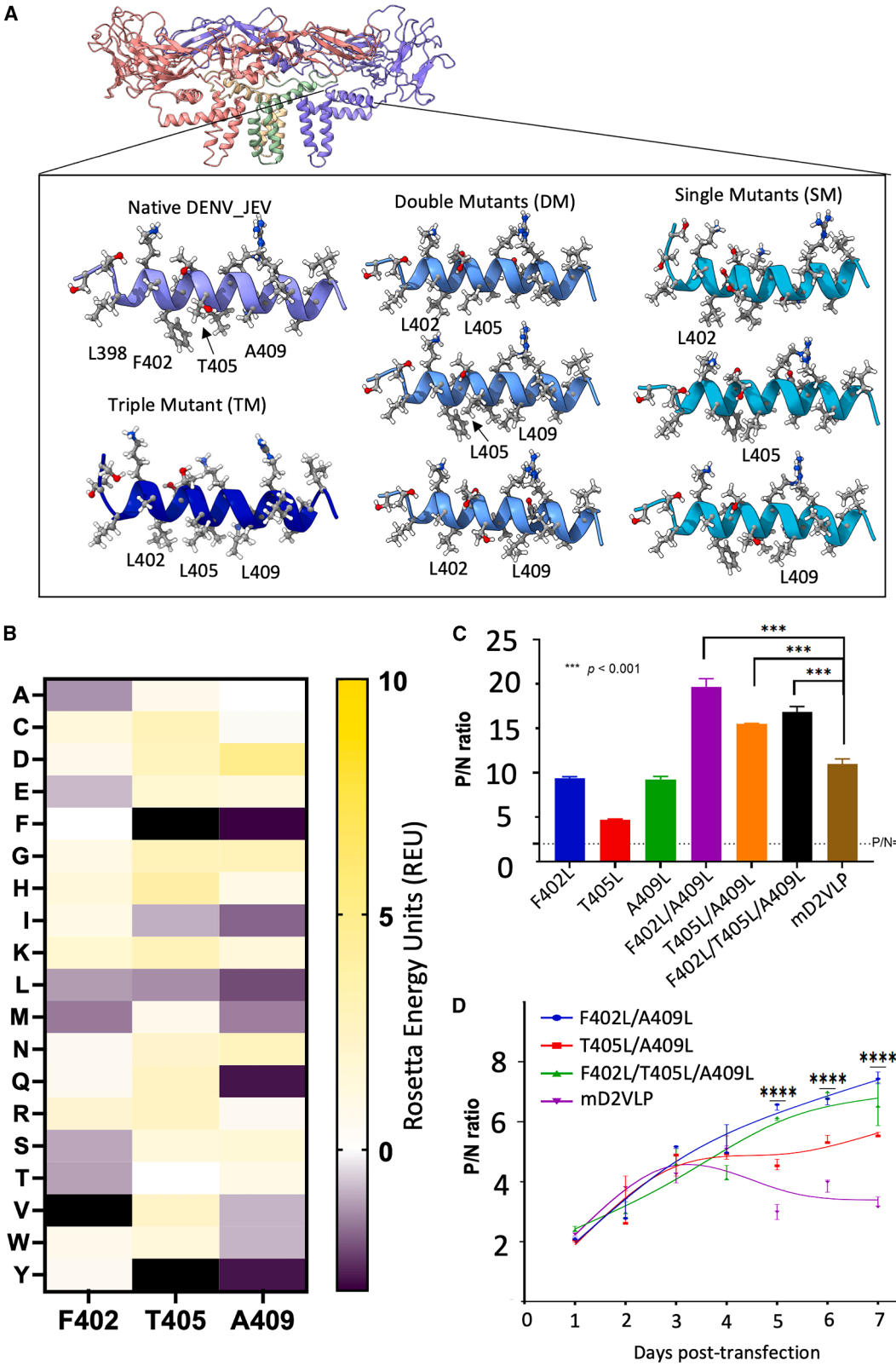

(legend on next page)

of native protein-protein quaternary interactions and the lipid envelope. We used a CG simulation approach to explore the dynamics of the entire VLP over physiologically relevant conditions and timescales. A protein shell consisting of 30 E-M dimeric units was constructed by fitting the AA protein structures into the lower-resolution cryo-EM density map of the VLP (EMDB:6926) and embedding into a lipid vesicle with an ~90-Å radius guided by the corresponding density (see the methods section for details). A total of six VLP models were built based on two vesicle lipid compositions (i.e., PL-dominant [VLP_{PL}] or DG-dominant [VLP_{DG}] membranes), each with three alternatives for the number of lipids packed into the vesicle (VLP_{PL}-1, VLP_{PL}-2, VLP_{PL}-3, and VLP_{DG}-1, VLP_{DG}-2, VLP_{DG}-3) (Figures 7A and 6B).

Each VLP model was first subjected to a 500-ns equilibration simulation, during which the position of protein backbone beads were restrained. This allowed lipid molecules to freely rearrange around the E-M protein shell, adopting a stable configuration inside the region of density for the lipid envelope indicated by the low-resolution cryo-EM map. In the VLP_{PL} systems, the lipid molecules became uniformly distributed around the protein shell (Figure 7C). In the VLP_{DG} systems, the spontaneous formation of lipid "bulges" or a local increase in bilayer thickness at specific regions was observed, as shown by calculations of headgroup density distributions (Figure 7D). This difference appeared to be due to DG molecules accumulating in the space between the bilayer leaflets of the vesicle, resulting in bulge formation beneath the E-M protein shell. Multiple previous studies have reported the accumulation of neutral lipids such as DG between lipid bilayer leaflets, known as transbilayer activity.[29,30] To confirm that this difference arose from the presence of DG lipids, simulations of the lipid vesicles in the absence of the protein shell revealed that the dominant PL vesicles retained their spherical shape, whereas the dominant DG vesicles exhibited lipid bulge formation (Figure S12).

The final equilibrated frame of each VLP model was used to perform 2-μs-long unrestrained simulations, which were run in triplicate (Figures 7C, 7D, and S13A). Simulation of the VLP_{PL} and VLP_{DG} systems led to distinct effects in terms of VLP morphology (Figures 7C and 7D). The spherical shape of the VLP_{PL} was observed to be dependent on the total lipid number for VLP_{PL} models (Figures 7Bi–7C). The VLP_{PL}-2 and VLP_{PL}-3 systems exhibited a stable spherical shape throughout the simulation time, whereas VLP_{PL}-1, which had the highest number of lipid molecules, adopted an ellipsoidal shape, and the structural deviation was greater than that in the simulations with a spherical morphology (Figure 7C; Videos S4 and S5). The ellipsoidal models are consistent with the particle morphologies previously reported to be present in cryo-EM micrographs, unlike spherical reconstructed structures, due to averaging.[21] This approach helps to rationalize the significant number of nonspherical particles observed in negative stain images or cryo-EM electron micrographs of VLPs. In contrast, in all the VLP_{DG} systems, the lipid bulges that formed during equilibration further expanded, occupying a larger space in the interior of the VLPs underneath the protein shell (Figure 7D). These data emphasize that the lipid molecules incorporated into VLPs dictate their overall morphology and size.

Our previous work highlighted the presence of a groove at the E-protein dimer interface on mD2VLP, which is absent from the mature DENV virion, indicating that VLPs potentially present unique epitope signatures to prime host immunity.[21] Therefore, we characterized the structural changes in the surface-exposed structural domains of the E protein (DI, DII, and DIII). The changes in intra/inter-E-protein dimeric contacts as a result of inherent molecular motions of VLPs are masked in a low-resolution structure; therefore, MD simulations allowed us to capture the changes in domain exposure from each VLP model system. To characterize epitope site exposure in mD2VLPs, we calculated the solvent accessible surface area (SASA) of DI, DII, and DIII (Figures S13B–S13D; Table S4). Each VLP model trajectory showed distinct propensities for domain exposure, which was in line with the morphological heterogeneity discussed above. Additionally, the SASA values at the starting state (t = 0 ns) and the mean SASA values over the simulation time of the domains from each VLP model system were compared (Table S4). Here, the VLP_{PL}-1 model with the highest lipid content in its vesicle showed the greatest exposure of all three domains, compared to the other VLP_{PL} models, indicating that overpacking of lipid molecules results in the disruption of native contact between E dimers. Furthermore, calculations of the average distance between DIIIs at each of the 12 sites of 5-fold symmetry axes lying diametrically opposite each other showed that DIIIs were more stable for the VLP_{PL} systems in comparison to VLP_{DG} systems (Figures S13E and S13F). Consistent with these findings, calculations of the distances between all 30 E-protein dimers revealed that the interdimer interfaces in VLP_{PL}-1 fluctuated the most (Figure S14A). In contrast, the domain SASAs and interdimer stability were far more uniform in the VLP_{DG} systems, suggesting that the bulging phenomenon in the DG-dominant vesicles may serve to "buffer" the particle size and better maintain the optimal arrangement of the DENV virion's native E-protein shell for antibody generation. Also, we performed principal-component

Figure 5. Engineering VLPs with enhanced secretion

(A) The side of view of dimerinc E-M protein shown in a cartoon representation, with the inset highlighting SH-1 (E-H1) from the native DENV-JEV E protein along with single, double, and triple mutants. Protein side chains are shown in liquorice representation.

(B) Heatmap showing the change in Rosetta energy units (REUs) upon mutation to any of the 19 amino acids (proline excluded) along critical E-H1 helix sites (i.e., residues 402, 405, and 409).

(C) Secretion assay comparing the efficacy of secreted Echi and its mutations (i.e., single/double/triple-Leu mutations in the E-H1 helix). Data are presented for terminal day 5. Statistical analysis of a two-tailed Student's t test was performed to determine significant differences between groups, with levels of significance defined by $^{****}p < 0.0001$ and $^{***}p < 0.001$.

(D) Daily secretion efficacy of wild-type and double/triple-mutant VLPs from day 1 to day 7 from HEK293 cell line. Statistical analysis was performed to determine significant differences between mD2VLP and mutants, with $p < 0.05$ indicating statistically significant variation for day 5–7. In (C) and (D) the mean values were calculated across three independent experiments, and the error bars correspond to standard deviation (SD).

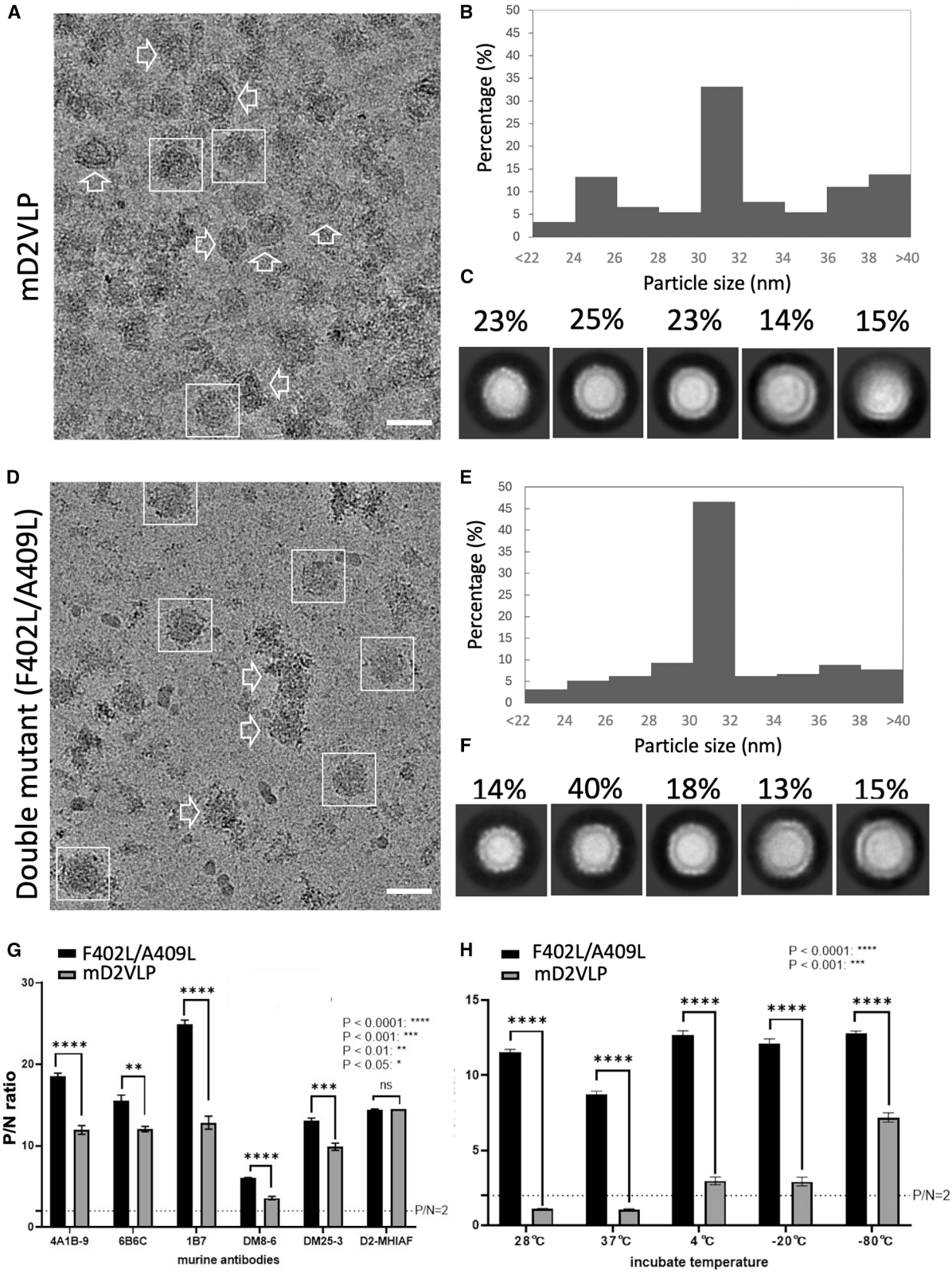

(legend on next page)

analysis (PCA) on the whole VLP to capture the most dominant motions. PCA1 revealed large-scale motion, which supported the morphological changes observed during the simulation (Figures S14B and S14C).

We further investigated the protein-lipid interactions between native DENV serotype 2 (VLP^{N}-1 and VLP^{N}-2) and chimeric (VLP_{PL}-1 and VLP_{PL}-2) VLPs using AA (E-M dimers embedded in PL and DG-dominant lipid bilayers) (Figures S15A–S15C) and CG-MD simulations (Figures S15D–S15F). Our simulations highlighted the critical differences in the SH-TM (residue 395–495) region with lipid interactions in both dimeric AA-MD and fully assembled VLP-CG MD simulations (Figure S15), which contributed to the differences in secretion levels reported previously. Furthermore, a comparison of the sequences of the SH-TM regions of native DENV and JEV revealed that the JEV (chimeric) sequence consists of more crucial hydrophobic residues, such as leucine and phenylalanine, which favor prominent lipid interactions (Figure S16). Overall, our VLP-CG simulations reveal the role of E-M protein shell-lipid interactions in influencing morphology and modulating VLP dynamic motion and epitope exposure.

DISCUSSION

A major challenge in dengue vaccine development lies in generating neutralizing antibodies against all four serotypes while closely mimicking the morphology of mature virions, with minimal risk of ADE. VLPs, which can form spontaneously during orthoflavivirus infection, have long been explored as a promising vaccine platform. However, the design of orthoflavivirus VLPs must account for the assembly process and yield, which vary significantly across expression systems and often result in VLPs of differing conformation, size, and physical properties.[22] Past work on orthoflavivirus VLPs—including DENV, WNV, and ZIKV—has revealed broad heterogeneity in their size (15–60 Å) and shape. The structural characterization of DENV VLPs has been hampered by their inherent instability and the complex interactions between viral proteins and the lipid envelope. To address these challenges, we employed an integrated computational and experimental approach to engineering VLPs with enhanced morphology, homogeneity, secretion efficiency, and preserved immunogenicity.

We first focused on the interactions between the E protein and lipids within the VLP envelope, aiming to improve secretion. AA-MD simulations and experimental assays showed that the charge and hydrophobicity of the E-H1 helix are critical factors influencing VLP assembly. By introducing mutations distant from key epitopes and oriented toward the lipid bilayer, we enhanced VLP secretion *in vitro*. We observed ~2-fold increase in secretion with respect to chimeric mD2VLP and ~150-fold increase with respect to native DENV2 VLP from previous study.[23] Antibody-binding experiments confirmed that these mutations did not impair epitope exposure; on the contrary, the high-secreting double mutant exhibited improved antibody accessibility. This may reflect increased conformational stability or a more accessible antigen structure. Furthermore, thermal stability assays and ELISA consistently showed enhanced structural integrity and antibody binding for the double mutant, supporting its potential immunological advantages.

These improvements address a key bottleneck in large-scale VLP production, where low yields during downstream processing limit commercial viability. To explore the structural basis of these findings, we employed CG simulations to model full VLPs, enabling analysis of particle morphology and epitope presentation. In line with previous studies,[21,31] we observed substantial heterogeneity in VLP size (~26–36 nm) and shape (spherical to ellipsoidal). CG simulations using two lipid compositions, based on experimentally derived vesicles, helped dissect this variability. In DG-dominant systems, lipid bulges appeared to stabilize particle size irrespective of total lipid content, consistent with cryo-EM observations. In contrast, PL-dominant systems showed that total lipid content governed vesicle morphology, with a threshold number of lipids required to maintain a spherical structure.

Importantly, our simulations revealed that most VLPs are nonspherical and heterogeneous, aligning with experimental cryo-EM data. This underscores the potential of tuning protein-lipid interactions to reduce heterogeneity and present a diverse array of epitopes, thereby enhancing immune priming. Previous studies in ZIKV have similarly identified lipid-binding motifs at the SH-TM regions of prM and E proteins as critical for viral assembly.[32,33] Our lipidomics data highlight the complexity of vesicle composition, reinforcing the need to consider the biophysical and immunological roles of individual lipid species.

Comparative analysis of VLP dynamics under varying lipid compositions revealed differences in domain flexibility and epitope exposure, which likely influence immunogenicity. These findings align with recent studies showing that antigenic properties such as epitope spacing, exposure, and structural fluctuations can profoundly impact immune responses.[34] A comprehensive *in vivo* study is therefore warranted to evaluate the immunogenic potential of engineered VLPs in the context of different envelope lipid compositions.

The conserved herringbone-like arrangement of the E protein across orthoflaviviruses supports the feasibility of extending

Figure 6. Cryo-EM analysis, antigenicity, and stability of wild-type and double-mutant mature dengue VLPs

(A–F) Representative cryo-EM micrographs of wild-type and double-mutant mature dengue VLPs showing spherical particles (boxed) and irregular or incomplete structures (arrows) are shown in (A) and (D), respectively. The scale bar corresponds to 50 nm. Size distribution of wild-type and double-mutant samples are shown in (B) and (E). Selected 2D class averages of double-mutant and wild-type mature dengue VLPs were obtained through reference-free 2D classification using CryoSPARC v3, and are shown in (C) and (F). Particles ranging from 24 to 38 nm in size were included in the analysis.

(G) Comparing mD2VLP (wild type) and double-mutant VLP (F402L/A409L) binding to a panel of mAbs to assess the structural integrity of VLP epitopes.

(H) Probing stability of wild-type and double-mutant (F402L/A409L) VLP at various temperatures using antigen capture-ELISA with anti-dengue 2-mouse hyperimmune ascitic fluid (D2-MHIAF) pAb. VLPs were incubated for 7 days at respective temperatures prior to ELISA assay.

Statistical analysis of a two-tailed Student's t test was performed to determine significant differences between groups, with levels of significance defined by $^{****}p < 0.0001$, $^{***}p < 0.001$, and $^{**}p < 0.01$. In (G) and (H) the mean values were calculated across three independent experiments, and the error bars correspond to standard deviation (SD).

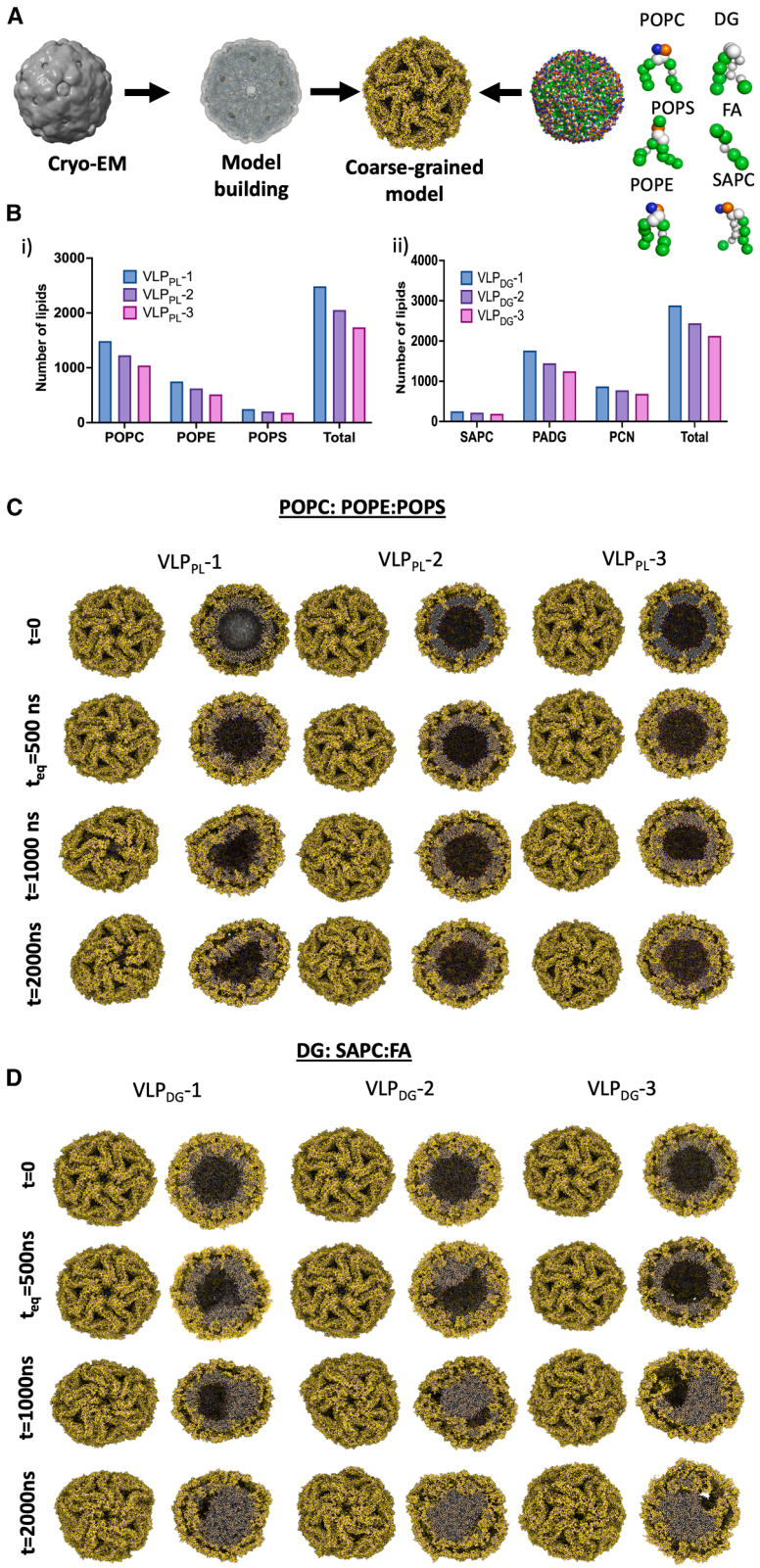

Figure 7. CG simulations of dengue VLPs

(A) Workflow of the construction of a CG model of DENV-2 VLPs using an experimentally derived cryo-EM density map (EMD:6926). The composition and number of lipid molecules in each VLP model are shown in (B). Simulation snapshots of VLPs with different lipid compositions are shown for the (C) PL-dominant and (D) DG-dominant VLP models. Snapshots are shown at progressive simulation time points for alternative models involving different amounts of lipids and membrane compositions. Each unrestrained simulation was performed in triplicate. VLP models showing the overall shape and cross section are shown in bead representations with protein components in yellow and lipid components in gray.

this VLP engineering strategy to other viruses such as ZIKV, JEV, and WNV. Large-scale production of biologics—including antibodies, vaccines, and VLPs—relies on optimizing production yields and cost-efficiency.[35] Key industrial strategies include cell-line selection, growth-condition optimization, and refinement of purification workflows.[36] Notably, neVLPs can self-assemble *in vitro*, while eVLPs typically require more complex maturation processes.

Our findings demonstrate that a small number of targeted mutations canenhance E-H1 helix insertion and lipid interactions as well as significantly improve VLP secretion, homogeneity while retaining immunogenicity. Exploring different lipid compositions may further improve yield and uniformity. Like infectious DENV particles, VLPs undergo a maturation process mediated by low pH and host proteases[21]; however, many VLPs remain immature due to inefficiencies in this process.[21] We previously introduced mutations at the prM furin cleavage site to shift this equilibrium toward mature forms.[22] Future efforts could optimize protein-lipid interactions during the immature stage to better control VLP properties, although the current lack of high-resolution structural data on immature DENV VLPs remains a barrier.

To overcome this, structural studies of VLP-Fab complexes offer a promising route. Fab binding may stabilize the VLP structure and reduce conformational fluctuations, thereby improving cryo-EM resolution and aiding in the elucidation of atomistic details of the E-M protein shell and lipid organization.

In conclusion, various strategies have been employed to develop orthoflavivirus VLPs as vaccine platforms, but relatively few have investigated their morphology and structural stability. Here, we demonstrate an integrated computational and experimental approach to engineer eVLPs with improved secretion and morphological homogeneity. Our study provides a proof of concept for applying this design strategy to other orthoflaviviruses such as ZIKV and JEV, paving the way for next-generation VLP-based vaccines.

METHODS

VLPs and mutants

Three different previously constructed and characterized recombinant DNA plasmids expressing prM-E of orthoflavivirus were used to generate VLPs from COS-1 cells (monkey fibroblast kidney tissue, ATCC #CRL-1650), namely mD2VLP, JEV, and ZIKV. Based on the protocol generated in our laboratory, as previously described,[37] the mD2VLP-expressing plasmid pVD2i-C18S was used to express prM, 80% of the E protein of DENV-2 (Asian one genotype, strain 16681), and 20% (from the carboxy-terminal end) of the E protein of JEV (Nakayama strain). The plasmid was previously modified at the furin cleavage site of prM to generate mature VLPs. Additionally, the pVD2i-C18S plasmid was used for site-directed mutagenesis following the manufacturer's protocol (Stratagene, La Jolla, CA). The primers used for site-directed mutagenesis are specified in Table S1. Traditional Sanger nucleotide sequencing confirmed that all the plasmids contained no mutations other than those indicated.

Equal quantities (4 μg) of plasmids expressing mD2VLP or mutant mD2VLPs were also transfected into HEK293T cells, which were subsequently seeded into 24-well plates (human embryonic kidney [ATCC]#CRL-3216) using branched polyethylenimine (PEI) (Sigma-Aldrich, St. Louis, MO, USA) with a PEI:DNA ratio of 1:1. The supernatant after transfection was harvested for antigen-capture ELISA up to day 5. Five days post transfection, the cells were fixed with 70% acetone for immunofluorescence (IFA) assays. To compare the expression kinetics of the mD2VLP and mutant VLPs, the plasmids were individually transfected into 293T cells, which were pre-seeded into 12-well plates, and the supernatants were collected daily from day 1 to day 7. To quantify the amount of different VLP antigens, we performed an antigen-capture ELISA.

Antigen-capture ELISA for VLP secretion, kinetics, and epitope mapping

The secretion of VLP-containing supernatant harvested from the plasmid-transfected cells was tested by antigen-capture ELISA as described previously.[21] Briefly, a 96-well ELISA plate (Thermo, #442404) was coated with in-house-prepared rabbit sera against D2VLP, ZIKV-VLP, or JEVLP diluted 1:500 in bicarbonate buffer (0.015 M Na_2CO_3 and 0.035 M $NaHCO_3$, pH 9.6) at 4°C overnight. Then, 50 μL of each transfected supernatant was added to each well and incubated at 37°C for 1 h. The pan-orthoflavivirus anti-E mAb FL0231 (a kind gift from Dr. L.-K. Chen, TzuChi University Hospital, Hualien, Taiwan) and the secondary antibody goat anti-mouse-IgG-HRP were added sequentially for detection. When comparing mD2VLP and mutant VLPs, 50 μL of anti-DENV-2 MHIAF antibody diluted 1:2,000 in blocking buffer was added to each well for antigen normalization. The optical density (OD) results for detection were reported according to the average positive-to-negative (P/N) ratio at 450/630 nm for each VLP sample. The 450- and 630-nm absorbance readings represent specific wavelengths of light used to measure the OD of a solution. While 450 nm is the primary wavelength for the colorimetric signal, the 630 nm is here used as a reference wavelength to measure the background noise and to correct for non-specific absorbance. Positive (P) values for each sample were calculated based on the average OD450 subtracted the average OD630 from the replicates that reacted with positive VLP antigens; whereas negative (N) values were calculated similarly from the replicates that reacted with culture medium control without transfection. The P/N ratio was computed after normalization to the negative control (NC_{cell}) obtained from the cell culture supernatant via mock transfection. A P/N value of greater than 2 for a given VLP sample was classified as secretion positive. When P/N ratio is close to 1, it suggests that the secretion levels observed in the transfected culture supernatant are almost identical to those of the supernatants without transfection, implying no detectable VLP secreted. Also, identical procedure was carried out to compare the particle stability of mD2VLP and double-mutant (F402L/A409L) VLPs post 7-day incubation at 37°C, 28°C, 4°C, −20°C, and −80°C with anti-DENV-2 MHIAF pAb.

Similar antigen-capture ELISAs were used to assess the epitope accessibility and structure integrity of mD2VLP and mutant, except that 1:100 dilutions of the specific mAb were used to replace MHIAF. First, equal amounts of D2VLP and mutant antigens, which were quantified based on the antigen titration curve reaching an equivalent P/N ratio, were added to the wells. A P/N ratio of 14 for both mD2VLP and mutant VLP

was selected to ensure an equivalent amount of both VLP antigens was applied to the wells. Accordingly, D2-MHIAF was also included as a positive control to confirm that differences in binding activity were not due to variations in antigen quantity. Second, a panel of well-characterized murine mAbs was used for epitope mapping, including group cross-reactive antibodies (4A1B-9, 6B6C-1) recognizing E protein of all four major pathogenic orthoflavivirus serocomplexes, sub-group cross-reactive antibodies (1B7-5) recognizing more than one orthoflavivirus serocomplexes, complex cross-reactive antibodies (DM25-3) recognizing all four serotypes of DENV serocomplex, and serotype-specific mAb (DM8-6) recognizing DENV-2 only. A helical wheel representation of JEV E-H1 (peptide 398–415) was generated using the NetWheels web application.[38]

IFA

HEK293T cells were transfected with plasmids expressing mD2VLP or mutant mD2VL to evaluate intracellular protein expression by IFA. Five days post transfection, the cells were fixed with 70% acetone at room temperature for 10 min. The cells were then blocked with 3% BSA at 37°C for 1 h. The same pan-orthoflavivirus anti-E mAb, FL0231, was added to the wells and incubated at 4°C overnight. Finally, the cells were washed three times and incubated for 1 h at 37°C with a mixture of fluorescein isothiocyanate-conjugated goat anti-mouse IgG (1:200; Jackson ImmunoResearch, West Grove, PA) and DAPI1:500; Invitrogen, Molecular Probes, Eugene, OR) diluted in 1% BSA in 1× PBS. After washing five times, the coverslips were mounted on glass slides and the cells were visualized under a fluorescence microscope (CKX41; Olympus).

Optimization of lipid-extraction methods

Three methods were used for lipid extraction of mD2VLP: chloroform extraction, alcohol (EtOH) extraction, and methyl tertiary butyl ether (MTBE) extraction. These lipid-extraction methods have previously been used to explore the lipid content in virus particles or VLPs.[39–41] Based on a literature search, the chloroform lipid-extraction approach is the most commonly used method, which is modified from the Bligh and Dyer or Folch lipid-extraction method.[42] Considering that the lipid composition of mD2VLP has never been explored before, we applied three different approaches to the same batch of purified mD2VLP and compared the yields of each method. Next, 10 μL of purified mD2VLPs from the HEK293T-transfected group (mD2VLPs) was subjected to lipid extraction by the following three different methods: (1) for chloroform extraction, 800 μL of 0.1 N HCl:CH_3OH (1:1) was added to the sample, followed by the addition of 400 μL of chloroform and shaking at 4°C for 1 min. The mixture was centrifuged at 16,000 × *g* for 7 min to separate the organic matter from the water phase. The lipid-containing organic layer was collected and dried under a chemical fume hood. (2) For EtOH extraction, 900 μL of acidic ethanol (0.18 M HCl: ethanol = 1:3) was added to the sample, which was subsequently subjected to low-temperature ultrasonic shaking for 3 min. Subseqently, the supernatant was collected after centrifugation at 14,000 × *g* at 4°C and dried under a vacuum concentrator. (3) For MTBE extraction, 225 μL of methanol at 4°C was added to the sample, which was subsequently vortexed for 10 s. Then, 750 μL of MTBE at 4°C was added to the sample, which was shaken for 6 min. The sample was centrifuged at 14,000 × *g* for 2 min by adding another 188 μL of ddH_2O and shaking for 20 s. The upper organic layer was collected and dried under a vacuum concentrator. All the dried samples were stored at −20°C and redissolved in 0.1% formic acid buffer before injection for LC-MS/MS analysis. The mock-transfected group (293T) was also subjected to lipid extraction as a negative control.

LC-ToF MS and lipidomic analysis

Liquid chromatography (LC) time-of-flight (ToF) MS was performed on a Waters ACQUITY UPLC I-Class system with a Xevo G2XS ToF mass spectrometer operated in positive- or negative-ion mode. The LC system consisted of a Waters ACQUITY UPLC system. Lipid molecules were separated on an ACQUITY UPLC BEH Amide column (150 × 2.1 mm; 1.7 μm) (Waters, Milford, MA, USA). The column was maintained at 45°C at a flow rate of 0.4 mL/min. Mobile phase A consisted of H_2O with 10 mM ammonium formate and 0.125% formic acid, and mobile phase B consisted of ACN/H_2O (95:5, v/v) with 10 mM ammonium formate and 0.125% formic acid. A sample volume of 0.5–3 μL was used for the injection. The separation of mobile phase B was conducted with the following gradient: 0 min 100%, 2 min 100%, 7.7 min 70%, 9.5 min 40%, 10.3 min 30%, 12.8 min 100%, and 17 min 100%. The sample temperature was maintained at 10°C. The MS scan range varied from 50 to 1,200 *m/z*. The desolvation nitrogen gas was set to 900 L/h at a temperature of 550°C, and the source temperature was set at 120°C. The capillary voltage and cone voltage were set to +2.5/−2 kV and 25 V, respectively. This chromatographic approach allowed effective separation of the different lipid species.[43] Three replicate analyses were performed for each group; first, a full mass scan was performed at 100–1,000 *m/z*, and the top 20 signals were selected according to the scan strength (the maximum number of candidate ions to monitor per cycle). Parent ions with a valence of 1 and a signal intensity greater than 30 cps were analyzed by tandem MS (MS/MS) sequentially through collision-induced dissociation (CID) and subsequently collected at 100–1,000 *m/z*. The exclusion time for precursor target ions was set at 6 s for data-dependent acquisition analysis (DDA). The parameters used were as follows: IonSpray voltage floating (ISVF), 5,500 V (ES+), −4,500 V (ES−); ion source gas 1 (GS1), 50; ion source gas 2 (GS2), 50; curtain gas (CUR), 27; and temperature (TEM), 450.

The lipidomic data of each VLP from each extraction method were subsequently collected by searching for *m/z* ratios against the online database LIPID MAPS (http://www.lipidmaps.org). The total sum of the *m/z* spectra of all lipid categories detected from purified mD2VLPs was calculated, and the lipid group extracted with chloroform had the largest sum of the total spectra obtained in the positive- or negative-ion scanning mode (Figure S1). Since the lipid extraction approach using chloroform was the most suitable lipid-extraction method based on the yield, the chloroform method was used to determine the lipid compositions of the different VLP preparations.

AA simulation system setup

E-protein dimers from dengue (gene ID: KU725663.1) and chimeric dengue (80% DENV, i.e., residues 1–394 and 20% JEV, i.e., residues 395–495) were modeled using Modeller version

9.10[44,45] with the PDB templates 3J27[26] and 5WSN,[46] respectively. The 100 models generated for each E-protein dimer and the structure with the lowest discreet optimized protein energy score and highest percentage of residues with dihedral angles in the allowed region of the Ramachandran plot were chosen for MD simulations. AA-MD simulations were performed in GROMACS-2018[47,48] using the CHARMM36m force field.[49] Native or chimeric or E-H1 helix mutant E-M protein dimers were embedded into two different lipid membrane systems composed of either POPC:POPE:POPS or DAG:POPC:FA (POPC is 1-palmitoyl-2-oleoyl-*glycero*-3-phosphatidylcholine [16:0/18:1]; POPE is 1-palmitoyl-2-oleoyl-*glycero*-3-phosphatidylethanolamine [16:0/18:1]; POPS is 1-palmitoyl-2-oleoyl-*glycero*-3-phosphatidylserine [16:0/18:1]; DAG is diacylglycerol [18:0/20:4]; SAPC is 1-stearol-2-arachidonoyl-phosphatidylcholine [18:0/20:4]; and FA is oleic acid [18:1]). Lipid bilayers were built using the CHARMM-GUI Membrane Builder,[50,51] and ratios of the number of lipid molecules were obtained from the current and previous studies. A 60:30:10 ratio of the number of molecules on the phospholipid (PL) dominant membrane (POPC:POPE:POPS) was reported for a native viral membrane,[52] and a DG-dominant lipid membrane (DG:SAPC:FA) ratio of 56:26:8 was used as per the lipidomic data from the present study. The orientation of the E-M protein dimers with respect to the lipid bilayers was predicted using the Orientation of Proteins in Membranes (OPM) reference server.[53] Dimeric E-M protein-lipid bilayer systems were solvated with ~66,000 TIP3P[54] water molecules in a 16.6 × 16.6 × 12.2 nm^3 box and a physiological salt solution of 150 mM NaCl (Table S2) in addition to neutralizing the overall system charge. Single, double, and triple mutations at sites 402, 405, and 409 on the chimeric E protein were modeled using the CHARMM-GUI PDB Reader & Manipulator tool.[55] The E-M protein-lipid membrane mixture was subjected to 5,000 steps of steepest descent minimization with a 0.01 nm step size. The minimized systems were subjected to multiple steps of equilibration, with position restraints applied to the protein backbone atoms and lipid head groups, and the initial force constants gradually decreased from 4,000 to 0 kJ mol^{-1} nm^{-2} and 2,000 kJ mol^{-1} nm^{-2}, respectively. The force constants were gradually reduced over a total of 1.5 ns of equilibration simulation, performed first in the NVT ensemble with a 1-fs time step followed by the NPT ensemble with a 2-fs time step. Integration was performed using the leapfrog algorithm. Semi-isotropic Berendsen pressure[56] coupling at 1 bar was used during equilibration, while a temperature of 303.15 K was maintained using the Berendsen thermostat. Each system production simulation was run for 500 ns without any restraints. The particle mesh Ewald (PME) method[57,58] was used for long-range electrostatic interactions, with a real space cutoff distance of 1.2 nm, and van der Waals interactions were set to a 1.2-nm cutoff distance with a force-switching function applied at 1 nm. The Nosé-Hoover thermostat (303 K)[59] and semi-isotropic Parrinello-Rahman barostat[60] (1 bar) with 1- and 5-ps coupling constants were used for the production runs, respectively. Trajectory visualization and analysis, including RMSDs, solvent accessibility,[61] PCA,[62] and secondary structure,[63] were performed using VMD[64] version 1.9.3 along with GROMACS tools.

The RosettaMP module was used to predict the ΔΔG of Echi protein mutants. The protocol described by Alford et al. (2015) was used in the present study.[27,65] Briefly, Echi-M dimer protein structures oriented according to the OPM database were used. The input pdb file was cleaned and renumbered using *clean_pdb.py* (from Rosetta scripts), and span files were generated using the *span_from_pdb* application in the RosettaMP module. To assess the effect of point mutations on SH-1 of the E protein, the MPddG module was used, with a fixed backbone prediction protocol and the franklin2019 scoring function.[66,67] Side-chain conformations were sampled for residues within 8 Å of the mutation position, and the ΔΔG was calculated using Rosetta energy units (REUs) between the mutant and native structures. Mutants with favorable predicted ΔΔG values (i.e., negative) were subjected to MD as described above, and their secretion efficiency was experimentally tested.

DENV wild-type and double-mutant VLP purification

The mD2VLPs and F402/A409 double mutant (mutant) were produced by transfecting HEK293T cells with the recombinant pVD2i-C18S plasmid and the mutant plasmid, using the Lipofectamine 2000 DNA Transfection Reagent (Thermo Fisher Scientific, USA). The culture supernatants were harvested and subjected to purification via 5%–25% sucrose gradient centrifugation in TNE buffer (50 mM Tris-HCl, 100 mM NaCl, 1 mM EDTA) using a Beckman SW-41 Ti swinging-bucket rotor. Fractions with the highest OD values in the ELISA assay were collected, and the VLPs were resuspended in TNE buffer. To further concentrate the samples, Amicon Ultra-0.5 centrifugal filter units with a 100-kDa cutoff were used.

Cryo-EM data collection and image analyses

Fresh samples were immediately applied to glow-discharged Quantifoil grids (Quantifoil, Germany) for cryo-EM grid preparation. Excess liquid was blotted off, and the grids were rapidly vitrified in liquid-nitrogen-cooled liquid ethane using a Vitrobot Mark IV (Thermo Fisher Scientific). Cryo-EM images were acquired at a magnification of 81,000× and an accelerating voltage of 300 kV, using an FEI Titan Krios transmission electron microscope equipped with a K3 detector (super-resolution mode). The pixel size at the specimen level was 1.061 Å/pixel. Image processing and 2D classification were conducted using CryoSPARC v3.[68] A total of 7,204 and 7,373 particles from the mD2VLP and mutant samples, respectively, were selected for heterogeneity analysis. The particles, ranging in size from 15 to 50 nm, were included in the analysis process.

SDS-PAGE

The purity of mD2VLP and mutant VLP was characterized by SDS-PAGE. The purified VLPs were first measured by Bradford assay as described previously,[21] and ~1 μg of both purified VLPs were denatured by adding β-mercaptoethanol, followed by boiling at 100°C 5 min. The samples were subjected to 4%–20% SDS-PAGE followed by Coomassie blue staining for 30 min and destained for 2 h. The E protein with molecular weight approximately 50 kDa was quantified by ImageJ (v1.52).

CG simulation setup

ChimeraX[69,70] was used to construct a fully assembled atomistic model of the VLPs with 60 E-M proteins fitted into the cryo-EM

density map of mature DENV-2 VLPs (EMDB:6926).[21] The fully assembled VLP structure consists of 30 E-M protein dimers embedded in a lipid vesicle.[71] The AA coordinates of the E-M proteins assembled in the VLP structure were converted to a Martini3 CG model[72] using the *martinize.py* script available in the vermouth python module. To retain the native fold, an elastic network (EN) was introduced within each E and M protein monomer. The EN was applied between pairs of beads within a cutoff range of 0.5–0.9 nm using a force constant of 1.000 kJ mol^{-1} nm^{-2}. The EN was applied only within each domain (DI, DII, and DIII) of the E-protein ectodomain, while the secondary structure of the E and M protein TM regions was maintained using standard angle and dihedral potentials. The CG E-M protein shell of the VLP was embedded into a lipid vesicle with a radius of ~90 Å (as per the approximate density of lipids observed in the cryo-EM map) by superimposing the centers of mass of the protein shell and lipid vesicle. Lipid vesicles were generated using the CHARMM-GUI Martini marker[73] with different lipid compositions guided by experimentally identified compositions. The protocol for embedding E-M proteins into lipid vesicles has been described elsewhere.[71] After embedding the E-M protein shell into the respective lipid vesicle, lipid molecules with coordinates overlapping with the protein beads were removed. Multiple initial CG VLP models were generated with different numbers of lipids by removing lipid molecules at 0.1, 0.15, and 0.2 nm from one another, corresponding to the $VLP_{PL/DG}$-1, $VLP_{PL/DG}$-2, and $VLP_{PL/DG}$-3 systems, respectively. Each VLP model was centered in a cubic box and solvated with MARTINI water along with solvated sodium and chloride beads corresponding to a 150 mM NaCl concentration.

All the systems were subjected to energy minimization of 50,000 steps using the steepest descent algorithm and 0.01 nm ste size. All the simulations were performed using GROMACS version 2018.[47,48] In all the simulations, bond lengths were constrained using the linear constraint solver (LINCS) algorithm,[74] and equations of motion were integrated using the leap-frog algorithm and a 10-fs time step. Isotropic pressure of 1 bar was maintained using Berendsen barostat[56] while temperature was maintained at 310 K using velocity-rescaling thermostat[75]. Six sets of equilibration steps in the NVT and NPT ensembles were performed by gradually lowering the restraints applied to the position of protein and lipid beads while progressively increasing the time step. The final NPT equilibration step involved position restraints applied to protein beads for 500 ns. Unrestrained production runs of 2,000 ns were run in triplicate for each VLP CG system (Table S3). Furthermore, we performed PCA on the protein-backbone beads of the VLPs for each VLP system from the concatenated triplicate simulation trajectory of 6 μs.

RESOURCE AVAILABILITY

Lead contact

Requests for further information and resources should be directed to and will be fulfilled by the lead contact Jan K. Marzinek (marzinekj@bii.a-star.edu.sg) and Day-Yu Chao (dychao@dragon.nchu.edu.tw).

Materials availability

All plasmids generated in this study are available from the lead contact with a completed materials transfer agreement.

Data and code availability

- Data: all data generated and analyzed in this study are included in the article and its supplemental information. Any additional information required to reanalyze the data reported in this work is available from the lead contact upon request.
- Code: simulations and analysis were performed using freely available software as detailed in the methods section.
- Other items: additional materials, including input parameter files and detailed protocols, are available from the lead contact upon request.

ACKNOWLEDGMENTS

The computational work for this article was fully performed on resources of the National Supercomputing Center, Singapore (https://www.nscc.sg). The cryo-EM experiments were performed at the Academia Sinica Cryo-EM Facility (ASCEM) in Taiwan. This work also used ASGC (Academia Sinica Grid-computing Center) Distributed Cloud resources, which is supported by Academia Sinica.

Funding was received from A*STAR AME Young Individual Research Grant (YIRG) number A2084c0160, the National Research Foundation Competitive Research Programme (NRF-CRP27-2021-0003), Bioinformatics Institute (BII) A*STAR core funds, and the National Science and Technology Council (112-2320-B-006 -022 -MY3) in Taiwan.

AUTHOR CONTRIBUTIONS

Conceptualization, J.K.M. and D.-Y.Z.; methodology, J.K.M., P.J.B., S.-R.W., D.-Y.Z., and V.R.P.; investigation, V.R.P., F.-C.C., and G.-W.C.; supervision, J.K.M., D.-Y.Z., and P.J.B.; writing – original draft, V.R.P., J.K.M., P.J.B., S.-R.W., and D.-Y.Z.

DECLARATION OF INTERESTS

The findings reported in this manuscript are protected under [Patent Application No. PCT/SG2024/050717] and are the subject of a patent application filed by Agency for Science, Technology and Research (A*STAR) in Singapore.

SUPPLEMENTAL INFORMATION

Supplemental information can be found online at https://doi.org/10.1016/j.xcrp.2025.102814.

Received: March 11, 2025
Revised: July 25, 2025
Accepted: August 13, 2025
Published: September 9, 2025

REFERENCES

1. Bhatt, S., Gething, P.W., Brady, O.J., Messina, J.P., Farlow, A.W., Moyes, C.L., Drake, J.M., Brownstein, J.S., Hoen, A.G., Sankoh, O., et al. (2013). The global distribution and burden of dengue. Nature *496*, 504–507.
2. Bashir, A. (2023). How climate change is changing dengue fever. Br. Med. J. *382*, 1690.
3. Postler, T.S., Beer, M., Blitvich, B.J., Bukh, J., de Lamballerie, X., Drexler, J.F., Imrie, A., Kapoor, A., Karganova, G.G., Lemey, P., et al. (2023). Renaming of the genus Flavivirus to Orthoflavivirus and extension of binomial species names within the family Flaviviridae. Arch. Virol. *168*, 224.
4. Lim, X.X., Chandramohan, A., Lim, X.Y.E., Bag, N., Sharma, K.K., Wirawan, M., Wohland, T., Lok, S.M., and Anand, G.S. (2017). Conformational changes in intact dengue virus reveal serotype-specific expansion. Nat. Commun. *8*, 14339.
5. Zhang, X., Sheng, J., Austin, S.K., Hoornweg, T.E., Smit, J.M., Kuhn, R.J., Diamond, M.S., and Rossmann, M.G. (2015). Structure of acidic pH dengue virus showing the fusogenic glycoprotein trimers. J. Virol. *89*, 743–750.

6. Durbin, A.P., and Whitehead, S.S. (2011). Next-generation dengue vaccines: novel strategies currently under development. Viruses *3*, 1800–1814.

7. Wan, Y., Shang, J., Sun, S., Tai, W., Chen, J., Geng, Q., He, L., Chen, Y., Wu, J., Shi, Z., et al. (2020). Molecular Mechanism for Antibody-Dependent Enhancement of Coronavirus Entry. J. Virol. *94*, e02015-19.

8. Rey, F.A., Stiasny, K., Vaney, M.C., Dellarole, M., and Heinz, F.X. (2018). The bright and the dark side of human antibody responses to flaviviruses: lessons for vaccine design. EMBO Rep. *19*, 206–224.

9. Morrone, S.R., and Lok, S.M. (2019). Structural perspectives of antibody-dependent enhancement of infection of dengue virus. Curr. Opin. Virol. *36*, 1–8.

10. World Health Organization. Updated Questions and Answers related to the dengue vaccine Dengvaxia. https://www.who.int/groups/global-advisory-committee-on-vaccine-safety/topics/dengue-vaccines/safety-update.

11. Fatima, K., and Syed, N.I. (2018). Dengvaxia controversy: impact on vaccine hesitancy. J. Glob. Health *8*, 010312.

12. Biswal, S., Borja-Tabora, C., Martinez Vargas, L., Velásquez, H., Theresa Alera, M., Sierra, V., Johana Rodriguez-Arenales, E., Yu, D., Wickramasinghe, V.P., Duarte Moreira, E., Jr., et al. (2020). Efficacy of a tetravalent dengue vaccine in healthy children aged 4-16 years: a randomised, placebo-controlled, phase 3 trial. Lancet *395*, 1423–1433.

13. Biswal, S., Reynales, H., Saez-Llorens, X., Lopez, P., Borja-Tabora, C., Kosalaraksa, P., Sirivichayakul, C., Watanaveeradej, V., Rivera, L., Espinoza, F., et al. (2019). Efficacy of a Tetravalent Dengue Vaccine in Healthy Children and Adolescents. N. Engl. J. Med. *381*, 2009–2019.

14. Rivera, L., Biswal, S., Sáez-Llorens, X., Reynales, H., López-Medina, E., Borja-Tabora, C., Bravo, L., Sirivichayakul, C., Kosalaraksa, P., Martinez Vargas, L., et al. (2022). Three-year Efficacy and Safety of Takeda's Dengue Vaccine Candidate (TAK-003). Clin. Infect. Dis. *75*, 107–117.

15. Mohsen, M.O., and Bachmann, M.F. (2022). Virus-like particle vaccinology, from bench to bedside. Cell. Mol. Immunol. *19*, 993–1011.

16. Nooraei, S., Bahrulolum, H., Hoseini, Z.S., Katalani, C., Hajizade, A., Easton, A.J., and Ahmadian, G. (2021). Virus-like particles: preparation, immunogenicity and their roles as nanovaccines and drug nanocarriers. J. Nanobiotechnol. *19*, 59.

17. Prates-Syed, W.A., Chaves, L.C.S., Crema, K.P., Vuitika, L., Lira, A., Côrtes, N., Kersten, V., Guimarães, F.E.G., Sadraeian, M., Barroso da Silva, F.L., et al. (2021). VLP-Based COVID-19 Vaccines: An Adaptable Technology against the Threat of New Variants. Vaccines (Basel) *9*, 1409.

18. Sainsbury, F., Cañizares, M.C., and Lomonossoff, G.P. (2010). Cowpea mosaic virus: the plant virus-based biotechnology workhorse. Annu. Rev. Phytopathol. *48*, 437–455.

19. Ueda, G., Antanasijevic, A., Fallas, J.A., Sheffler, W., Copps, J., Ellis, D., Hutchinson, G.B., Moyer, A., Yasmeen, A., Tsybovsky, Y., et al. (2020). Tailored design of protein nanoparticle scaffolds for multivalent presentation of viral glycoprotein antigens. eLife *9*, e57659.

20. Glasgow, J.E., Capehart, S.L., Francis, M.B., and Tullman-Ercek, D. (2012). Osmolyte-mediated encapsulation of proteins inside MS2 viral capsids. ACS Nano *6*, 8658–8664.

21. Shen, W.-F., Galula, J.U., Liu, J.H., Liao, M.Y., Huang, C.H., Wang, Y.C., Wu, H.C., Liang, J.J., Lin, Y.L., Whitney, M.T., et al. (2018). Epitope resurfacing on dengue virus-like particle vaccine preparation to induce broad neutralizing antibody. eLife *7*, e38970.

22. Thoresen, D., Matsuda, K., Urakami, A., Ngwe Tun, M.M., Nomura, T., Moi, M.L., Watanabe, Y., Ishikawa, M., Hau, T.T.T., Yamamoto, H., et al. (2024). A tetravalent dengue virus-like particle vaccine induces high levels of neutralizing antibodies and reduces dengue replication in non-human primates. J. Virol. *98*, e0023924.

23. Purdy, D.E., and Chang, G.J.J. (2005). Secretion of noninfectious dengue virus-like particles and identification of amino acids in the stem region involved in intracellular retention of envelope protein. Virology *333*, 239–250.

24. Veena Rani, N., Kapoor, N., and Krishnan, A. (2023). Efficient generation and characterization of chimeric dengue viral-like particles. Biochem. Biophys. Res. Commun. *654*, 10–17.

25. Urakami, A., Ngwe Tun, M.M., Moi, M.L., Sakurai, A., Ishikawa, M., Kuno, S., Ueno, R., Morita, K., and Akahata, W. (2017). An Envelope-Modified Tetravalent Dengue Virus-Like-Particle Vaccine Has Implications for Flavivirus Vaccine Design. J. Virol. *91*, e01181-17. https://doi.org/10.1128/jvi.01181-17.

26. Zhang, X., Ge, P., Yu, X., Brannan, J.M., Bi, G., Zhang, Q., Schein, S., and Zhou, Z.H. (2013). Cryo-EM structure of the mature dengue virus at 3.5-Å resolution. Nat. Struct. Mol. Biol. *20*, 105–110.

27. Alford, R.F., Koehler Leman, J., Weitzner, B.D., Duran, A.M., Tilley, D.C., Elazar, A., and Gray, J.J. (2015). An Integrated Framework Advancing Membrane Protein Modeling and Design. PLoS Comput. Biol. *11*, e1004398.

28. Salem, G.M., Galula, J.U., Wu, S.R., Liu, J.H., Chen, Y.H., Wang, W.H., Wang, S.F., Song, C.S., Chen, F.C., Abarientos, A.B., et al. (2024). Antibodies from dengue patients with prior exposure to Japanese encephalitis virus are broadly neutralizing against Zika virus. Commun. Biol. *7*, 15.

29. Campomanes, P., Zoni, V., and Vanni, S. (2019). Local accumulation of diacylglycerol alters membrane properties nonlinearly due to its transbilayer activity. Commun. Chem. *2*, 72.

30. Skinner, J.R., Shew, T.M., Schwartz, D.M., Tzekov, A., Lepus, C.M., Abumrad, N.A., and Wolins, N.E. (2009). Diacylglycerol enrichment of endoplasmic reticulum or lipid droplets recruits perilipin 3/TIP47 during lipid storage and mobilization. J. Biol. Chem. *284*, 30941–30948.

31. Metz, S.W., Thomas, A., White, L., Stoops, M., Corten, M., Hannemann, H., and de Silva, A.M. (2018). Dengue virus-like particles mimic the antigenic properties of the infectious dengue virus envelope. Virol. J. *15*, 60.

32. DiNunno, N.M., Goetschius, D.J., Narayanan, A., Majowicz, S.A., Moustafa, I., Bator, C.M., Hafenstein, S.L., and Jose, J. (2020). Identification of a pocket factor that is critical to Zika virus assembly. Nat. Commun. *11*, 4953.

33. Goellner, S., Enkavi, G., Prasad, V., Denolly, S., Eu, S., Mizzon, G., Witte, L., Kulig, W., Uckeley, Z.M., Lavacca, T.M., et al. (2023). Zika virus prM protein contains cholesterol binding motifs required for virus entry and assembly. Nat. Commun. *14*, 7344.

34. Ellis, D., Dosey, A., Boyoglu-Barnum, S., Park, Y.J., Gillespie, R., Syeda, H., Hutchinson, G.B., Tsybovsky, Y., Murphy, M., Pettie, D., et al. (2023). Antigen spacing on protein nanoparticles influences antibody responses to vaccination. Cell Rep. *42*, 113552.

35. Buckland, B.C. (2005). The process development challenge for a new vaccine. Nat. Med. *11*, S16–S19.

36. Vicente, T., Roldão, A., Peixoto, C., Carrondo, M.J.T., and Alves, P.M. (2011). Large-scale production and purification of VLP-based vaccines. J. Invertebr. Pathol. *107*, S42–S48.

37. Galula, J.U., Chang, G.-J.J., and Chao, D.-Y. (2019). Production and Purification of Dengue Virus-like Particles from COS-1 Cells. Bio. Protoc. *9*, e3280.

38. Mól, A.R., Castro, M.S., and Fontes, W. (2018). NetWheels: A web application to create high quality peptide helical wheel and net projections. Preprint at bioRxiv. https://doi.org/10.1101/416347.

39. Ivanova, P.T., Myers, D.S., Milne, S.B., McClaren, J.L., Thomas, P.G., and Brown, H.A. (2015). Lipid Composition of the Viral Envelope of Three Strains of Influenza Virus—Not All Viruses Are Created Equal. ACS Infect. Dis. *1*, 435–442.

40. Schlotterbeck, J., Chatterjee, M., Gawaz, M., and Lämmerhofer, M. (2019). Comprehensive MS/MS profiling by UHPLC-ESI-QTOF-MS/MS using SWATH data-independent acquisition for the study of platelet lipidomes in coronary artery disease. Anal. Chim. Acta *1046*, 1–15.

41. Cajka, T., and Fiehn, O. (2017). LC–MS-Based Lipidomics and Automated Identification of Lipids Using the LipidBlast In-Silico MS/MS Library. In

Lipidomics: Methods and Protocols, S.K. Bhattacharya, ed. (New York, NY: Springer New York), pp. 149–170.

42. Bligh, E.G., and Dyer, W.J. (1959). A rapid method of total lipid extraction and purification. Can. J. Biochem. Physiol. *37*, 911–917.
43. Tsugawa, H., Ikeda, K., Takahashi, M., Satoh, A., Mori, Y., Uchino, H., Okahashi, N., Yamada, Y., Tada, I., Bonini, P., et al. (2020). A lipidome atlas in MS-DIAL 4. Nat. Biotechnol. *38*, 1159–1163.
44. Sali, A., and Blundell, T.L. (1993). Comparative protein modelling by satisfaction of spatial restraints. J. Mol. Biol. *234*, 779–815.
45. Eswar, N., John, B., Mirkovic, N., Fiser, A., Ilyin, V.A., Pieper, U., Stuart, A. C., Marti-Renom, M.A., Madhusudhan, M.S., Yerkovich, B., and Sali, A. (2003). Tools for comparative protein structure modeling and analysis. Nucleic Acids Res. *31*, 3375–3380.
46. Wang, X., Li, S.H., Zhu, L., Nian, Q.G., Yuan, S., Gao, Q., Hu, Z., Ye, Q., Li, X.F., Xie, D.Y., et al. (2017). Near-atomic structure of Japanese encephalitis virus reveals critical determinants of virulence and stability. Nat. Commun. *8*, 14.
47. Van Der Spoel, D., Lindahl, E., Hess, B., Groenhof, G., Mark, A.E., and Berendsen, H.J.C. (2005). GROMACS: fast, flexible, and free. J. Comput. Chem. *26*, 1701–1718.
48. Berendsen, H.J.C., van der Spoel, D., and van Drunen, R. (1995). GROMACS: A message-passing parallel molecular dynamics implementation. Comput. Phys. Commun. *91*, 43–56.
49. Huang, J., Rauscher, S., Nawrocki, G., Ran, T., Feig, M., de Groot, B.L., Grubmüller, H., and MacKerell, A.D., Jr. (2017). CHARMM36m: an improved force field for folded and intrinsically disordered proteins. Nat. Methods *14*, 71–73.
50. Jo, S., Kim, T., Iyer, V.G., and Im, W. (2008). CHARMM-GUI: a web-based graphical user interface for CHARMM. J. Comput. Chem. *29*, 1859–1865.
51. Jo, S., Kim, T., and Im, W. (2007). Automated builder and database of protein/membrane complexes for molecular dynamics simulations. PLoS One *2*, e880.
52. Zhang, Q., Hunke, C., Yau, Y.H., Seow, V., Lee, S., Tanner, L.B., Guan, X. L., Wenk, M.R., Fibriansah, G., Chew, P.L., et al. (2012). The stem region of premembrane protein plays an important role in the virus surface protein rearrangement during dengue maturation. J. Biol. Chem. *287*, 40525–40534.
53. Lomize, M.A., Pogozheva, I.D., Joo, H., Mosberg, H.I., and Lomize, A.L. (2012). OPM database and PPM web server: resources for positioning of proteins in membranes. Nucleic Acids Res. *40*, D370–D376.
54. Mark, P., and Nilsson, L. (2001). Structure and Dynamics of the TIP3P, SPC, and SPC/E Water Models at 298 K. J. Phys. Chem. A *105*, 9954–9960.
55. Park, S.-J., Kern, N., Brown, T., Lee, J., and Im, W. (2023). CHARMM-GUI PDB Manipulator: Various PDB Structural Modifications for Biomolecular Modeling and Simulation. J. Mol. Biol. *435*, 167995.
56. Berendsen, H.J.C., Postma, J.P.M., van Gunsteren, W.F., DiNola, A., and Haak, J.R. (1984). Molecular dynamics with coupling to an external bath. J. Chem. Phys. *81*, 3684–3690.
57. Darden, T., York, D., and Pedersen, L. (1993). Particle mesh Ewald: An N·log(N) method for Ewald sums in large systems. J. Chem. Phys. *98*, 10089–10092.
58. Essmann, U., Perera, L., Berkowitz, M.L., Darden, T., Lee, H., and Pedersen, L.G. (1995). A smooth particle mesh Ewald method. J. Chem. Phys. *103*, 8577–8593.
59. Evans, D.J., and Holian, B.L. (1985). The Nose–Hoover thermostat. J. Chem. Phys. *83*, 4069–4074.
60. Parrinello, M., and Rahman, A. (1981). Polymorphic transitions in single crystals: A new molecular dynamics method. J. Appl. Phys. *52*, 7182–7190.
61. Eisenhaber, F., Lijnzaad, P., Argos, P., Sander, C., and Scharf, M. (1995). The double cubic lattice method: Efficient approaches to numerical integration of surface area and volume and to dot surface contouring of molecular assemblies. J. Comput. Chem. *16*, 273–284.
62. Amadei, A., Linssen, A.B., and Berendsen, H.J. (1993). Essential dynamics of proteins. Proteins *17*, 412–425.
63. Kabsch, W., and Sander, C. (1983). Dictionary of protein secondary structure: Pattern recognition of hydrogen-bonded and geometrical features. Biopolymers *22*, 2577–2637.
64. Humphrey, W., Dalke, A., and Schulten, K. (1996). VMD: visual molecular dynamics. J. Mol. Graph. *14*, 27–38.
65. Leaver-Fay, A., Tyka, M., Lewis, S.M., Lange, O.F., Thompson, J., Jacak, R., Kaufman, K., Renfrew, P.D., Smith, C.A., Sheffler, W., et al. (2011). ROSETTA3: an object-oriented software suite for the simulation and design of macromolecules. Methods Enzymol. *487*, 545–574.
66. Kellogg, E.H., Leaver-Fay, A., and Baker, D. (2011). Role of conformational sampling in computing mutation-induced changes in protein structure and stability. Proteins *79*, 830–838.
67. Chaudhury, S., Lyskov, S., and Gray, J.J. (2010). PyRosetta: a script-based interface for implementing molecular modeling algorithms using Rosetta. Bioinformatics *26*, 689–691.
68. Punjani, A., Rubinstein, J.L., Fleet, D.J., and Brubaker, M.A. (2017). cryoSPARC: algorithms for rapid unsupervised cryo-EM structure determination. Nat. Methods *14*, 290–296.
69. Pettersen, E.F., Goddard, T.D., Huang, C.C., Meng, E.C., Couch, G.S., Croll, T.I., Morris, J.H., and Ferrin, T.E. (2021). UCSF ChimeraX: Structure visualization for researchers, educators, and developers. Protein Sci. *30*, 70–82.
70. Goddard, T.D., Huang, C.C., Meng, E.C., Pettersen, E.F., Couch, G.S., Morris, J.H., and Ferrin, T.E. (2018). UCSF ChimeraX: Meeting modern challenges in visualization and analysis. Protein Sci. *27*, 14–25.
71. Marzinek, J.K., Holdbrook, D.A., Huber, R.G., Verma, C., and Bond, P.J. (2016). Pushing the Envelope: Dengue Viral Membrane Coaxed into Shape by Molecular Simulations. Structure *24*, 1410–1420.
72. Souza, P.C.T., Alessandri, R., Barnoud, J., Thallmair, S., Faustino, I., Grünewald, F., Patmanidis, I., Abdizadeh, H., Bruininks, B.M.H., Wassenaar, T.A., et al. (2021). Martini 3: a general purpose force field for coarse-grained molecular dynamics. Nat. Methods *18*, 382–388.
73. Qi, Y., Ingólfsson, H.I., Cheng, X., Lee, J., Marrink, S.J., and Im, W. (2015). CHARMM-GUI Martini Maker for Coarse-Grained Simulations with the Martini Force Field. J. Chem. Theor. Comput. *11*, 4486–4494.
74. Hess, B., Bekker, H., Berendsen, H.J.C., and Fraaije, J.G.E.M. (1997). LINCS: A linear constraint solver for molecular simulations. J. Comput. Chem. *18*, 1463–1472.
75. Bussi, G., Donadio, D., and Parrinello, M. (2007). Canonical sampling through velocity rescaling. J. Chem. Phys. *126*, 014101.